Degradation Simulation and Investigation of Environmental Effects on Hybrid Halide Perovskite Degradation

Hongbo Qiao

A thesis

submitted in partial fulfillment of the

requirements for the degree of

Master of Science

University of Washington

2020

Reading Committee:

Hugh W. Hillhouse

Fumio S. Ohuchi

Program Authorized to Offer Degree:

Materials Science and Engineering

University of Washington

Abstract

Degradation Simulation and Investigation of Environmental Effects on Hybrid Halide Perovskite Degradation

Hongbo Qiao

Chair of the Supervisory Committee:
Hugh W. Hillhouse

The hybrid perovskite is an emerging material for photovoltaic application that reached 25.2% efficiency up to date. Intensive researches have focused on this area. Recently, understanding various degradation mechanism for HPs is catching more attention among researchers. In this work, we used a state of art technology to simultaneously measure the diffusion length, transmissivity, and photoluminescence intensity and take PL video. By combining the degradation results on spin coated $CsPbI_3$ and $MAPbI_3$ films, and spray coated $MAPbI_3$ film with a python simulation, we find a strong agreement that the $MAPbI_3$ degradation follows the mass loss mechanism. And we proposed a very detailed PL-PC-Tr experiments on spin cast $MAPbI_3$ films. With different levels of relative humidity, excitation intensity, temperature and gas environment, we reveled the influence of different environmental factors on degradation process. It is shown that temperature

combined with oxygen percentage is a dominant factor in the degradation process for $MAPbI_3$. We also find that the influence of high relative humidity is much more obvious at lower temperature. And excitation intensity with oxygen appear to exacerbate degradation at high temperature but not as effective at lower cases.

TABLE OF CONTENTS

LIST OF FIGURES

LIST OF TABLES

ACKNOWLEDGEMENTS

This work won't be possible without the countless help both from my research life and personal life along the way.

First, I would like to thank my professor, Dr. Hugh W. Hillhouse, for let me join the group and give me guidance through my master program. His enthusiasm in learning and research impressed me a lot, and this cheers me up every time when I face difficulties.

Second, I would like to express my gratitude to the all the Hillhouse's group members, especially Dr. Wiley Dunlap-Shohl, Dr. Ryan Stoddard, Yuhuan Meng and Jason Moore, who offered countless help not only for research, but also in daily life. Without their help, I would not be able to understand various of techniques and basic theories for perovskite fabrication and data interpretation. And they create a super friendly atmosphere in the group, and shows great patience when leading me the way, which gave me a huge confidence in life.

Then I would like to thank my parents, who give the financial support for me to studying aboard. Without their help, the whole story won't start. And thanks for their understanding the inconvenience caused by the distance and 15 hours jet lag.

Finally, I would like to thank all my friends across different countries. They cheer me up when I'm down, push me keep forward when I'm being lazy, and light the way when I lost in the fog.

Chapter 1. INTRODUCTION

In the 21st century, the energy crisis and environmental pollution are among the most significant problems the world needs facing. How to develop environmentally friendly and renewable energy and then to alleviate the energy crisis is the major issue that needs to be resolved shortly. Luckily, solar energy, clean and renewable energy, is not only rich in resources and free to use but also almost everywhere in the world, which means there is no need for transportation. It does not harm the environment and is easy to convert and use due to the rapidly developed solar technology. At present, there are two major ways to utilize solar energy, one is transferring the light to heat, and the other one is PV (photovoltaic), which converts the solar radiation into electrical energy. The fundamental element that can convert light to electricity is called solar cells. How to use low-cost solar cells to achieve a long lifetime and high-power conversion efficiency is always a hot spot in the PV field.

Among all types of solar cells, the silicon-based solar cell is undoubtedly the earliest and well-developed technology. Although the power conversion efficiency can be as high as 27.6%, people are still looking to an alternative product due to its high manufacturing costs. For this reason, the second-generation solar cell has been developed. This kind of thin-film solar cell is made by depositing one or more thin film of photovoltaic materials on the substrate. The thin-film technology requires fewer materials and is easy to fabricate more giant cells, which can effectively reduce the costs. However, efficiency is not as high as the silicon-based solar cells. Therefore, as technology developed, the third generation of solar cells has been made. This generation of solar cells combines the advantages of high efficiency, low costs, and large-area fabrication. The emerging photovoltaics include such as copper zinc tin sulfide solar cell (CZTS), hybrid organic-

inorganic perovskite solar cell, quantum dot solar cell, etc. Among these kinds of solar cells, the hybrid organic-inorganic perovskite solar cell has drawn people's attention due to its simple structure and cheap costs. This kind of solar cell was then developed in 2009 by Miyasaka with an efficiency of 3.8%[1], and with only ten years of development, the highest efficiency is achieved 25.2%[2] as shown in Figure 1.1.

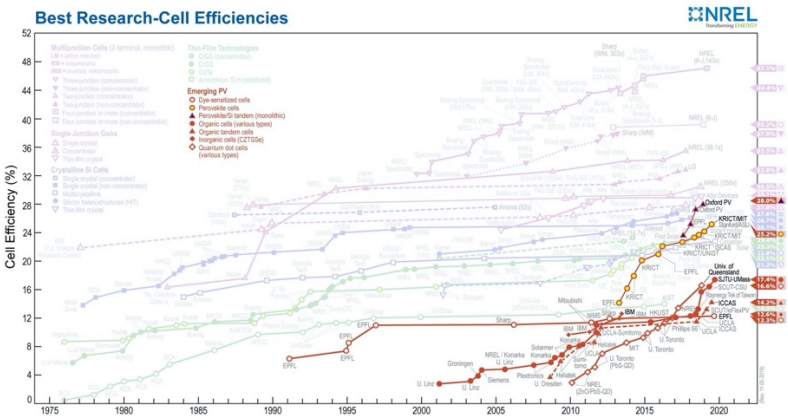

Figure 1.1 The record of PCE in emerging PV technology by NREL. This plot is courtesy of the National Renewable Energy Laboratory, Golden, CO.

1.1 HYBRID ORGANIC-INORGANIC PEROVSKITE

1.1.1 *Crystal Structure*

Perovskite, in general, is the materials with ABX_3 structure, as shown in Figure 1.2. The monovalent A+ site can be inorganic, such as Cs^+, or organic, such as $CH_3NH_3^+$ (MA^+) or $HC(NH_2)_2^+$ (FA^+), or a combination of them. And for most hybrid perovskite, the divalent B^{2+} site is always Pb^{2+}, and the X^- site is halogen anion, such as Cl^-, Br^- or I^-.[3] And to better understanding how the ions fit into the structure, Goldschmidt quantified the tolerance factor equation in 1926

$$t = \frac{r_A + r_B}{\sqrt{2}(r_A + r_B)} \quad (1.1)^4$$

Where r_A is the radius of A-site cation, r_B is the radius of the B site cation, and r_0 is the radius of the anion, and t, the tolerance factor, is defined as the ratio of the distance between A site and X site to the distance between B site to the X site in an idealized solid-sphere model. For cubic structure, the tolerance factor should be within 0.9 to 1, and for the orthorhombic structure, it should with 0.71 - 0.9. Based on this equation, we can verify if the combination of different cations and anions can form an ideal cubic perovskite phase or not. In general, the selection of B site cation follows the octahedral equation[4], but for hybrid perovskite, the cation B has universally been Pb. Because the other potential B site cation Sn generally has lower stability[5].

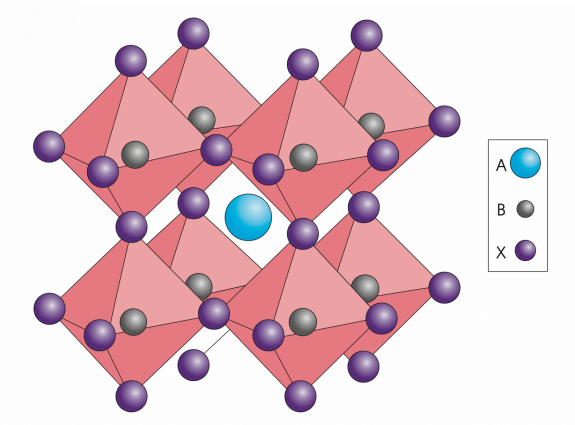

Figure 1.2 The crystal structure of ABX_3 perovskite.[3] Reprinted with permission from Springer Nature Customer Service Centre GmbH [Ref. 3]. Copyright © 2014

One of the most popular hybrids organic-inorganic perovskite is methylammonium lead iodide($MAPbI_3$), and due to its small A site cation, the tolerance factor is 0.91[6], which falls into the range of 0.8 to 1.0, which is believed an ideal material for forming the perovskite structure. However, the tolerance factor is not the only criterion, sometimes when the A site too large to fit in, the low dimensional perovskite can be formed, such as 0D, 1D, and 2D structure.[7] Moreover, for the low dimensional perovskite, the aliphatic and aromatic ammonium salt is the most commonly used to form the A-site cation.

1.1.2 *Electronic Structure*

For the photovoltaic devices, one of the most crucial property is the density of state, which is highly related to the optoelectronic properties for such materials, such as the recombination mechanisms, mobility, and intrinsic carrier concentration. For materials like $MAPbI_3$, a typical 3D perovskite, and $(C_4H_9NH_3)_2PbI_4$, a 2D perovskite material, the bonding diagram of the valence band and the conduction band is shown in Figure 1.3.

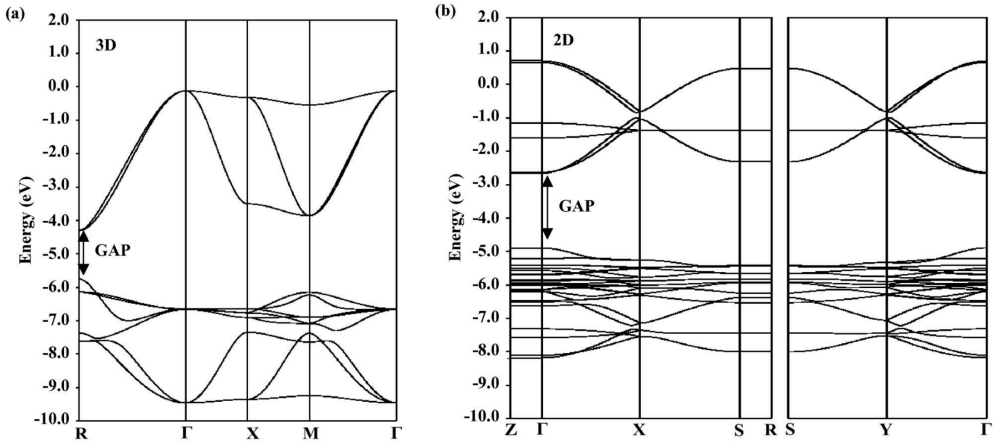

Figure 1.3 DFT calculated band structure of $MAPbI_3$ and $(C_4H_9NH_3)_2PbI_4$.[8] Reprinted figure with permission from [Ref.8] Copyright (2003) by the American Physical Society

1.1.3 *Tunable optoelectronic properties*

Another reason that hybrid perovskite draws people's attention is because of their highly tunable bandgap. The bandgap can be easily tuned through composition engineering by merely changing the composition and mixing different elements for each site. Take $CsPbI_3$ for instance, the emission spectra can vary from 410nm to 700nm, which means the emission energy varies from 1.77eV to 3.02eV by changing and mixing the X site with Cl, Br or I in different ratio as shown in Figure 1.4a[9]. And As shown in Figure 1.4b, by simply replacing the MA+ with FA+, the emission energy

E_g can vary from 1.61eV to 1.51eV[10], which shows the hybrid perovskite is an excellent potential light-absorbing material for application in solar cells.

Besides the tunable bandgap, the other two significant criteria for whether a material is a good light absorber are the carrier diffusion length (L_d) and the mobility. The hybrid perovskite thin films, like $MAPbI_3$ thin film, have incredibly high charge carrier mobility and relatively high diffusion length with a value as high as 10um for single crystal[11]. This large value of diffusion length highly exceeds the absorption depth of the photons that the perovskite can absorb, which leads to a high theoretically efficiency of solar cells. Due to all the advanced properties mentioned above, the hybrid perovskite has been proven to be a promising material in the application of optoelectronic filed, as shown in Figure 1.1, with the proved efficiency exceeding 25%.

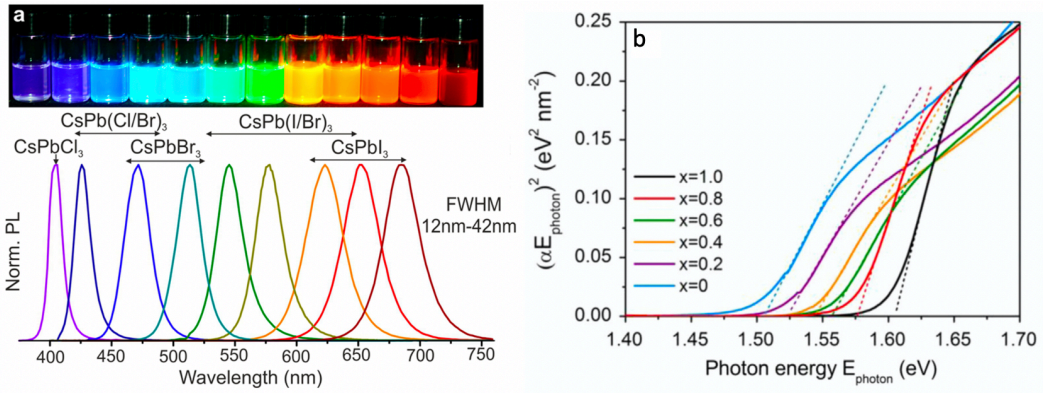

Figure 1.4 (a)Photoluminescence of $CsPbX_3$(X=Cl, Br, and I) nanocrystals showing the band[9]. Adapted with permission from [Ref. 9], Copyright (2015), American Chemical Society. (b)Kubelka-Munk spectra of $MA_XFA_{1-X}PbI_3$, where α is the absorption coefficient and E_{photon} is photon energy[10]. Reprinted from [Ref. 10], Copyright (2016), with permission from Elsevier.

1.2 CURRENT RESEARCH

Even the hybrid perovskite has a lot of advantages and is one of the most important photovoltaic materials. However, there are a couple of severe problems that occurred during the thin film

fabrication process, the pinhole formation, low crystallinity, and the phase inhomogeneity. These problems are the main reasons that have a terrible impact on the carrier lifetime and eventually influence the device performance. In the past few years, people mostly devoted to the study of improving the film quality and finally increasing the efficiency of perovskite solar cells. But recently, the research focus has slightly shifted to the degradation mechanism investigation[12,13]. Since the lifetime for a qualified solar cell should longer than 20 years, but the current record for perovskite solar cell is only years. The current research for three major environmental impacts are discussed below.

1.2.1 *Humidity Stability*

It is believed that the perovskite can absorb water very easily due to the ABX_3 structure if they are not encapsulated very well[14]. Unfortunately, moisture is one of the most pervasive harmful impactors to perovskite stability. Most of the materials will be driven to failure due to the presence of moisture, especially perovskite. Even now, people have developed several methods to encapsulate the solar cell in order to keep it away from moisture. It is still very important to know the mechanism behind the story. Several groups have used unencapsulated perovskite films and observed the degradation in air with high RH[15,16]. And it is believed that water penetrates the perovskite film very easily and then form hydrated perovskite in a short time. Several groups have tested the degradation of the $MAPbI_3$ film in a controlled RH environment and exposure time[15,17,18]. A consensus has been made that water can react with the $MAPbI_3$. Thus, the hydrates are formed. The formation equation that water is the only effect is shown in equation 1.2.

$$CH_3NH_3PbI_3 + H_2O \leftrightharpoons (CH_3NH_3)_4PbI_6 \cdot 2H_2O \qquad (1.2)$$

Alberti et al. have taken the following research that they observed that $MAPbI_3$ degradation in the high RH environment starts with a phase transition from tetragonal to cubic phase without

forming any hydrate, then followed by another phase change of PbI_2 formation[19]. Furthermore, Christians et al. found that when $MAPbI_3$ exposed to the artificially airtight humid atmosphere, which is created by mixing water and glycerol, only MA_4PbI_6-H_2O has formed[16]. Furthermore, Zhao et al. found that $MAPbI_3$ powder degradation was fully reversible if there is no loss of PbI_2 and MAI during the water evaporating procedure[20]. However, no matter what the degradation environment is, it is believed that the RH is highly related to the decomposition rate of the perovskite film. With high RH, the perovskite can fast transfer to PbI_2 and hydration with relatively short time contrast to the 10000h in 20% RH, which is reported by yang et al.[21]. Besides the influence on the composition, water affects the perovskite structure as well. Both calculations and experiments indicated that the grain boundaries and defects have a contribution to absorbing the water and generating more new grain boundaries, as shown in Figure 1.5[14]. Also, water in the perovskite crystals can form strong hydrogen bonds with organic cations[16], which leads to a deprotonation process and make the heat and light stress more active during the degradation.

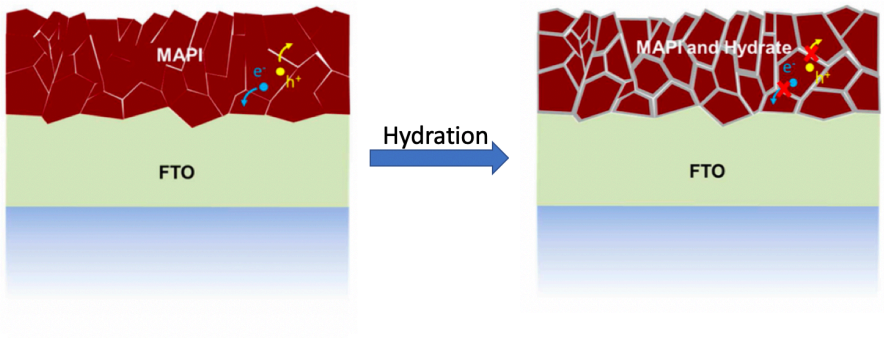

Figure 1.5 Microscopic degradation model of $MAPbI_3$ thin-film under partial hydration[14]

Adapted with permission from [Ref.14]. Copyright (2015) American Chemical Society.

1.2.2 *Thermal Affect*

The second most well-known stress that will affect film stability is heat. There are a couple of reasons why understanding thermal stability is very important. First, high temperature is required

in the process of fabricating solar cells. Most of the thin film fabrication method requires an annealing step at the end, and a lot of encapsulation procedure requires a temperature above 140 C. Second, the believed working temperature for most solar cells is above 65C in hot climates, and a lot of the accelerated stability test is using high temperature as a factor. Take $MAPbI_3$. For instance, this composition is not thermally stable even though it is much more structurally stable than $FAPbI_3$ and $CsPbI_3$ based on the tolerance factor discussed before. $MAPbI_3$ will be rapidly decomposition into PbI_2 and the FA composition will go through a rapid polymorphism[22]. In general, for $MAPbI_3$, the broad regime of this process is called organic sublimation. This thermal decomposition is believed to be followed by this reaction equation:

$$CH_3NH_3PbI_3 \rightarrow PbI_2 + CH_3NH_3^+ + I^- \quad (1.3)$$

The film will sublime the halide content first, followed by HI and MA evaporation, finally left the PbI_2. But there are still have some debate about what $CH_3NH_3^+$ and I^- will form, as shown in equation 1.4 and 1.5.[23]

$$CH_3NH_3^+{}_{(g)} + I^-{}_{(g)} \rightarrow CH_3NH_{2(g)} + HI_{(g)} \quad (1.4)$$

$$CH_3NH_3^+{}_{(g)} + I^-{}_{(g)} \rightarrow CH_3I_{(g)} + NH_{3(g)} \quad (1.5)$$

And Conings et al. found that the PbI_2 would form at the temperature as low as 85C in air, oxygen, and nitrogen, as shown in Figure 1.7.[24] As 85C is very close to the standard operating temperature 65C, the thermal stability is receiving increased attention these days.

Even with the substituting A site cation with such FA and Cs could obtain a more stable structure, but there are still some issues that happen, like pure $FAPbI_3$ shown in Figure 1.7. Partial substituting would work better and have much better stability because of the additional hydrogen bonding in FA[25]. And then it is hard for FA to release proton to forming HI with I^-.[26]. However, even partial substituting can improves the film stability a lot, McMeekin et al. report that the

believed very stable composition, (FA,Cs) $PB(I,Br)_3$ can start to degrade in an inert atmosphere at 130C within 6 hours[27]. With all the research have done in these years, people have found a decent but not perfect balance between the structure stability and decomposition stability and with a decent optoelectronic property by using the mixed cation and anion perovskite composition[28], but the mechanism still under development. There still are many kinds of research that need to be done for the degradation mechanism study.

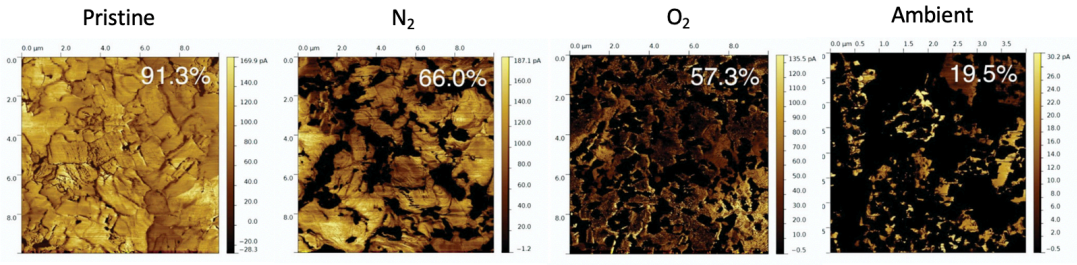

Figure 1.6 Conductive atomic force microscopy (c-AFM) images of $MAPbI_3$ films aged for 24 h in N_2, O_2, and ambient atmospheres. Percentages are the fraction of the area that conducts current. [24] Adapted with permission from [Ref. 24]. CC by John Wiley & Sons, Inc

1.2.3 *Oxygen and Light*

And the third majority stresses for the perovskite degradation are oxygen and illumination. In the previous research, people found that the metal halide perovskite is very stable in the oxygen when there is no illumination[29]. But when the film is under illumination, the perovskite can rapidly decompose[30] as shown in Figure 1.8. Snaith's group reported that the $MAPbI_3$ solar device would degrade about 20% under only 1sun illumination with exposed in oxygen within just a few hours[31]. Moreover, Haque et al. found that oxygen diffuse into the $MAPbI_3$ perovskite films immediately after the film exposed in the oxygen atmosphere and will be completely degraded with hours[32]. They think it is due to the oxygen molecular diffused into the iodide vacancies[32], and the iodide

vacancies in the pristine perovskite film are significantly high and can be generated quickly during the photoluminescence[33,34]. And once the vacancy is occupied by the oxygen molecular, the oxygen will trap the excited electrons around the conduction band and form O^{2-}, which is highly reactive superoxide and can react with the A-site cation to form H_2O. Then lead to the final failure of the film with the creation of PbI_2.

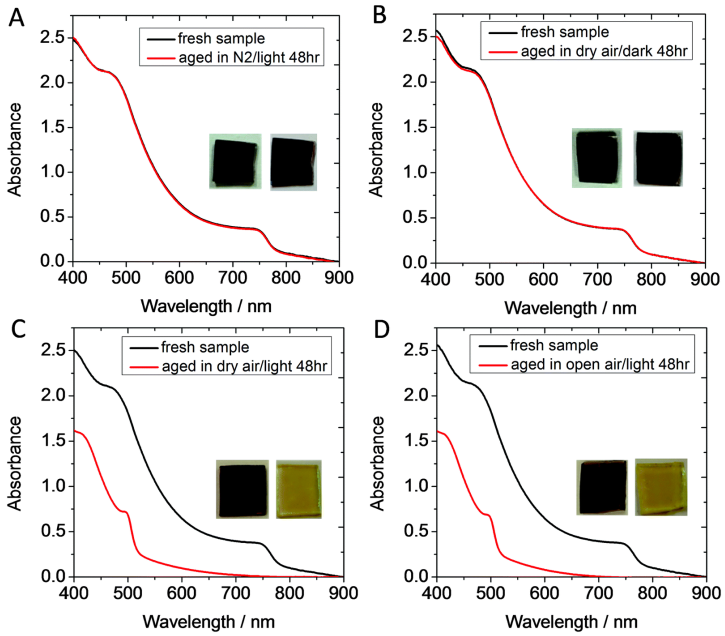

Figure 1.7 Absorption spectra for $MAPbI_3$ thin-films on glass before (black) and after (red). (a) films exposed to light under inert conditions. (b) films exposed to oxygen in the dark. (c) films exposed to both dry oxygen and light degrade. (d) films exposed to both oxygen and light degrade.[30] Reproduced by permission of The Royal Society of Chemistry

As we talked before, illumination is significant stress to accelerate the degradation process. Unlike the oxygen and humidity, which can be effectively kept away by encapsulating the device, the solar cells must work under illumination. This means the perovskite films must be intrinsically stable to light. Despite all the other factors mentioned above, when illumination is the only stress for the perovskite, people have found that there will be halide segregation, ion migration, and even

decomposition[33,35–37]. Like ion migration, DeQuilettes et al. have found that the photoluminescence intensity of $MAPbI_3$ films will increase at the beginning of under 1sun illuminated[37]. And as the researches go more and more in-depth, perovskite composition becomes more and more sophisticated in order to have a better band alignment and for exploring a better device. A new effect has been reported by Hoke et al., which is $AB(Br,I)_3$ perovskite films undergo reversible phase segregation into I- rich phase and Br- rich phase when it is exposed to light[35]. Hence this phenomenon is called the hoke effect, and this is the first evidence that the ion in perovskite film is mobile. This effect has drawn people's attention after it has been accepted. Since one of the most well-known uses for the hybrid perovskite is to tune the bandgap to around 1.7 eV, and the most attractive way to do that is to adjust the halide composition in the perovskite structure[38–40].As talked previously, people have worked a lot in how single stress affects the stability of perovskite films or devices, but only a few researches have done on the investigation of how multi stresses affect the perovskite film and what the mechanisms behind each story. This may due to the difficulty on creating such a degradation environment or exploring the mechanism straighter forward. Fortunately, by using a state of art instrument, it's becoming possible to visualize and quantify the perovskite degradation process. This paper is mainly focused on using this state of art instrument to investigate the degradation of $MAPbI_3$ composition perovskite films.

Chapter 2. METHODOLOGY

2.1 PHOTOLUMINESCENCE-PHOTOCONDUCTIVITY-TRANSMITTANCE(PL-PC-TR)

By combining the PL-PC-Tr method with the video analysis, photoluminescence quantum yield (PLQY), Quasi-Fermi level splitting (QFLS), diffusion length, and the remaining fraction of the perovskite phase remained in the film can be calculated and monitored simultaneously. Combining a video of the interesting area and device relevant optoelectronic properties in perovskite film is a very intuitive way to demonstrate the degradation process, and it is helpful to investigate the degradation mechanism afterward.

2.1.1 *Photoluminescence and video analysis*

PL is the light emission from the perovskite film after the absorption of photons. In this work, for most cases, PL refers to PLQY, which is the fraction of the number of emitted photons to the number of absorbed photons. This parameter is more commonly used to describe the performance of perovskite films. After obtained the PLQY, other crucial properties can be calculated, such as QFLS by applying equation 2.1[41]

$$\Delta E_F = \Delta E_{F,max} + kT \ln PLQY_{Ext} \quad (2.1)$$

where the $\Delta E_{F,max}$ is the Shockley-Queisser limit ΔE_F determined with bandgap extracted from UV-vis absorbance, and $PLQY_{Ext}$ is the spatial mean value collected by the wide-field PL microscopy, k is the Boltzmann constant and T is the absolute temperature. The wide-field microscopy, not like the confocal PL, can measure the spatial PL and take the images at the same time. From a time-series spatial PL data, a video can be obtained. By analyzing the three-dimensional data, a lot of information can be obtained, such as the spatial standard deviation of PLQY or QFLS, and the variance of these properties for each pixel alone the time. All these

properties are essential for tracking degradation through time as well as diffusion length, which will be discussed in the next section.

2.1.2 *Photoconductivity and diffusion length*

Only studying the PLQY is not sufficient to characterize the overall optoelectronic quality of a film. A film of nanocrystals with a passive surface can emit high PLQY, but may not be able to transport charge carriers to the contacts if there is no overlap between the carrier wave functions in adjacent nanocrystals[42]. Even this is a limiting case, quantifying carrier transport by measuring the effective diffusion length simultaneously with photoluminescence is under vital importance to describe the overall quality of a film. The lateral DC photoconductivity is measured to assess the carrier transport properties. The photoconductivity can be calculated by the equation below,

$$\sigma_{\mathrm{ph}} = \sigma_{\mathrm{l}} - \sigma_{\mathrm{d}} \tag{2.2}$$

where the σ_l is the conductivity under illumination, σ_d is in the conductivity in the dark[43]. And the relation between photoconductivity and mobility-lifetime product of the charge carriers is given by

$$\sigma_{\mathrm{ph}} = q\left(\mu_h p_{eff} + \mu_e n_{eff}\right) = qG(\mu_h \tau_h + \mu_e \tau_e) \tag{2.3}$$

where q is the elementary charge, $\mu_h$and μ_e are the mobility of hole and electron, G is the average volumetric photogeneration rate, p_{eff} and n_{eff} are effective nonequilibrium excess carrier concentration, and τ_h is the lifetime for free hole as well as the τ_e for free electron. Since the diffusion coefficient can be calculated as

$$D_{e,h} = \frac{kT\mu_{e,h}}{q} \tag{2.4}$$

And the diffusion length can be calculated by,

$$L_{e,h} = \sqrt{D_{e,h}\tau_{e,h}} \tag{2.5}$$

By combining these equations, and multiplying $kT/2q^2G$ photoconductivity equation above, mean diffusion length can be derived as below[43]

$$L_D = \sqrt{\frac{{L_e}^2+{L_h}^2}{2}} = \sqrt{\frac{\sigma_{ph}kT}{2q^2G}} \tag{2.6}$$

With a designed equipment, schematic shown in Figure 2.1, the photoconductivity can be carried out concurrently with time-dependent measurement of absolute intensity PL using a calibrated wide-field PL microscope[43]. it is worth to note that diffusion length in this work is the mean diffusion length described above, not the absolute diffusion length for electron or hole, which may differ significantly due to some reasons.

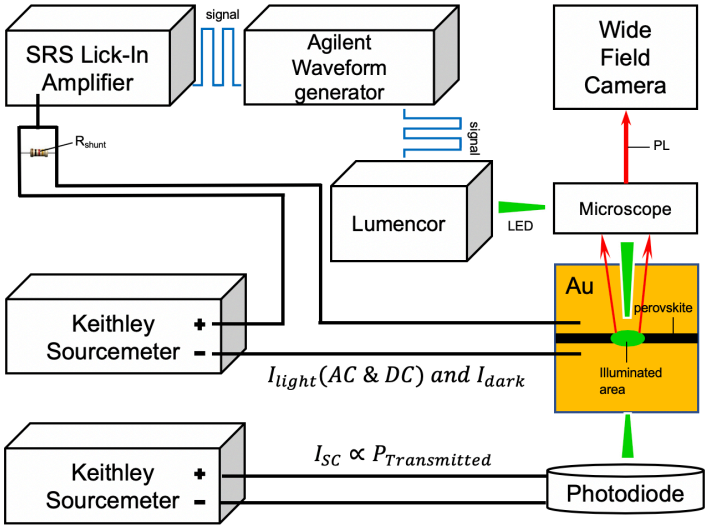

Figure 2.1 The schematic of PL-PC-TR Measurement

2.1.3 *Darkfield Microscopy*

Darkfield microscopy is a simple but effective technique to obtain a high contrast image of samples. Unlike the usual optical microscopy, darkfield microscopy doesn't show the natural color of the sample but shows it bright on a dark background. The difference of light path between darkfield

and bright is that there is a patch stop filter, which blocks the central light and leaves an outer ring of illumination. Then the light is focused to the sample by condenser as same as the brightfield. But then the scattered light is collected while the transmitted or directly reflected light (depends on the design of microscopy) simply stopped by the filter. The schematic is shown in the Figure 2.2

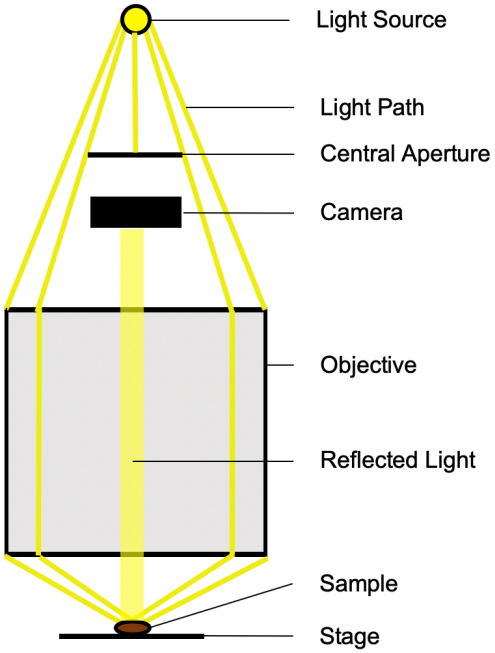

Figure 2.2 Light path for darkfield microscopy

2.2 Partial Differential Equation

Partial differential equations (PDEs) is widely used in solving diffusion questions, especially in solving two-dimensional heat diffusion questions. PDEs are functions that contains multivariable and their partial derivatives. A simple two-dimensional diffusion related PDE can be written as below,

$$\frac{\partial U}{\partial \mathrm{t}} = D\left(\frac{\partial^2 U}{\partial x^2} + \frac{\partial^2 U}{\partial y^2}\right) \tag{2.7}$$

where U is the concentration and D is the diffusion coefficient, and this function can be conducted from Fick's second law. A simple numerical approximation for $U(x, y, t)$ is to use discrete function $u_{i,j}^{(n)}$, where $t = i\Delta t, x = i\Delta x$ and $y = i\Delta y$ in the same range. By applying the finite approximation, the PDE can be written as,

$$\frac{u_{i,j}^{(n+1)} - u_{i,j}^{(n)}}{\Delta t} = D\left(\frac{u_{i+1,j}^{(n)} - 2u_{i,j}^{(n)} + u_{i-1,j}^{(n)}}{(\Delta x)^2} + \frac{u_{i,j+1}^{(n)} - 2u_{i,j}^{(n)} + u_{i,j-1}^{(n)}}{(\Delta y)^2}\right) \quad (2.8)$$

And the function can be rewritten as,

$$u_{i,j}^{(n+1)} = D\Delta t\left(\frac{u_{i+1,j}^{(n)} - 2u_{i,j}^{(n)} + u_{i-1,j}^{(n)}}{(\Delta x)^2} + \frac{u_{i,j+1}^{(n)} - 2u_{i,j}^{(n)} + u_{i,j-1}^{(n)}}{(\Delta y)^2}\right) + u_{i,j}^{(n)} \quad (2.9)$$

The post diffusion concentration in a 2D system can be calculated by this equation.

Chapter 3. EXPERIMENTS

3.1 HYBRID ORGANIC-INORGANIC PEROVSKITE FILM FABRICATION

For a better nucleation and film quality, people have developed a lot of ways to fabricate the perovskite film[44]. A schematic of frequently used methods is shown in Figure 3.1. Although among all these methods, the standard one-step solution process, which is also known as spin coating, is not as good as other methods in some ways, this method is still the simplest and most common one. In this paper, all perovskite films were made by spin coating methods with different parameters.

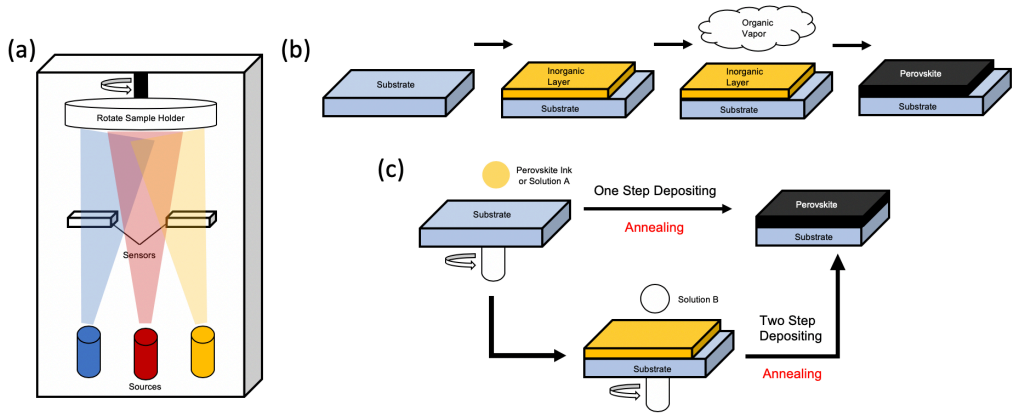

Figure 3.1 A schematic of three perovskite thin-film fabrication methods,(a) multi-source evaporation; (b) vapor-assisted solution (c) single and multi-steps solution processes.

3.1.1 *Ink Preparation*

Three compositions of ink are used in this work, $MAPbI_3$, $(FA_{.87}Cs_{.13})Pb(I_{.86}Br_{.14})_3$, and $CsPbI_3$. All of them have the same molarity, which is 1 mol/L. The $MAPbI_3$ solution is made by adding 0.3179g of MAI (Dyesol) and 0.922g PbI_2(Alfa Aesar) in a 20ml vial, which contains premixed NMP (N-Methyl-2-pyrrolidone, 99.5%, Sigma-Aldrich) and DMF (Dimethylformamide, 99.8%,

Sigma-Aldrich) with 1:1 ratio, and then put on the hot plate stirring for 90min with 550rpm at 70C. Similarly, the $(FA_{.87}Cs_{.13})Pb(I_{.86}Br_{.14})_3$ ink is made by adding 0.2885g FAI(Sigma-Aldrich), 0.0883g CsI(Sigma-Aldrich), 0.7284g PbI_2 and 0.1541 $PbBr_2$ (Alfa Aesar) in a 20ml vial, which contains premixed NMP and DMF with the ratio of 1:1 as well. The difference is after mixing the ink, the ink is put on the hot plate at 70C with 550 rpm for 3 hours, and will be filtered right before spin coating. The $CsPbI_3$ ink is made by mixing 0.5196g CsI and 0.922g PbI2 in a 20ml vial, which contains 2ml mixed DMF and DMSO(Dimethyl sulfoxide, 99.9%, Sigma-Aldrich) solution with the ratio of 4:1. Then 0.0216g zwitterion(3-(1-Pyridinio)-1-propane sulfonate, 99%, Acros Organics) is added to help to form perovskite phase during spin coating[45], and the ink is stirring on the hot plate at 80C with 550 rpm until mostly dissolved.

3.1.2 *Substrates Preparation*

Glass slides (VWR Vistavision Microscope Slides) are used to fabricate the film. The glass size is 75*25*1 mm, and the desired size for spin coating is 15*15*1 mm. Therefore, one glass slide is cut to 5 equal-sized pieces. Then the substrates go through four steps sonicate cleaning. These pieces are fit into a sample holder. Then the holder is put in a 500ml beaker, which is filled with different solutions for each step. The solutions used for each cleaning are powdered precision cleaner (Alconox) mixed with deionized water, deionized water, acetone (Fisher), IPA (Isopropyl alcohol, Fisher). Each step lasts for 10min. After the sonicating and right before the spin coating, samples are put in the Argon filled chamber for plasma cleaning about 10min. The glass substrate used for spray coating is slightly different from the spin-coated substrates on the size, which is 75*15*1 mm. After cutting, the sonicate and plasma cleaning steps are the same.

3.1.3 *Spin Coating Method*

In this paper, all the spin-coated film is fabricated with the Laurell WS-400BZ-6NPP/Lite spin coater. Right before the spin coating, blow the substrate surface with N_2 for removing the dust. For the MAPbI3 film, the spin coating recipe is adding 100ul ink on the substrate, then spinning at 4000rpm for 45s with the max accelerator, and then followed by dipping the substrate in DEE(Diethyl Ether, Anhydrous, Fisher) for 60s, then annealing at 100C for 10min on a hot plate. For the $(FA_{.87}Cs_{.13})Pb(I_{.86}Br_{.14})_3$, the recipe is adding 100ul ink on the substrate, then spinning coating at 4000rpm for 45s with the max accelerator, and use 700ul toluene(anhydrous, 99.8%, Sigma-Aldrich) for the anti-solvent wash at 12s remaining during the spin coating. A precut peptide tip is used during the anti-solvent wash. Then the annealing step is the same with $MAPbI_3$. And for the $CsPbI_3$, 100ul ink is added on the substrate then follows a 2-step spinning, 2000rpm for 2s, and 4000rpm for 35s. 580ul toluene anti-solvent wash is used at the 17s after starting. After the spinning, the substrate is annealed at 65C for 10 min and 90C for 20min.

3.1.4 *Spray Coating Method*

A single composition spray-coated sample is used in this work. One side of the substrate is prescribed into four 15*15 regions with a blank region on each side. Prescribing the substrate is for breaking the sample more easily before analyzing it. During the spraying, the sample is placed at the stage vertically. By adjusting the positioning laser next to the spray nozzle, make sure the substrate is located in the center of the spray region. Then perovskite ink is deposited via an ultrasonic spray nozzle at a constant speed of 150ul/min. The nozzle moves at 1mm/s along the vertical length of the spray area. After 1min dying, the sample is merged into DEE for anti-solvent wash about 60s, then followed by a 100C 10 min annealing.

3.1.5 *Evaporation*

A specifically designed mask is used to evaporate the gold contacts on the sample, as shown in Figure 3.2(b) the distance between the contacts can be adjusted by changing the wires across the middle of the slots. Each slot can perfectly fit in a spray-coated sample and can easily fit in four r spin-coated samples with carbon tape for fixing the location. In this work, the distance between contacts is 200um. And the Au contact depth is 80nm with the evaporation rate 2A/s. And the final structure of the sample which will be used to do the Photoluminescence-Photoconductivity-Transmittivity (PL-PC-TR) measurement is shown in Figure 3.2(a)

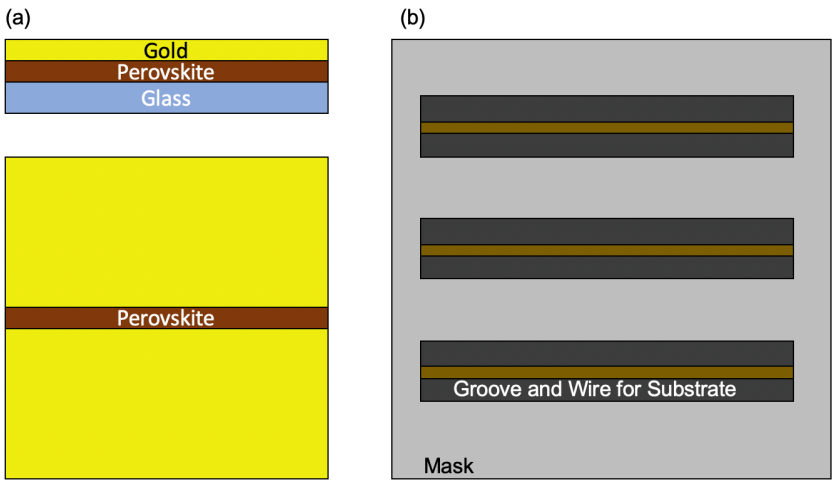

Figure 3.2 Schematic figure for the (a)structure(front and top view) of the sample, (b)bottom view of the mask.

3.2 UV-VIS CHARACTERIZATION

This method is used to measure the transmission and reflection of the thin film materials to further calculated the bandgap in this work. The optical absorbance spectra are collected from PerkinElmer Lambda 1050 UV/vis/NIR spectrometer with an integrating sphere in the laboratory atmosphere.

3.3 WIDE-FIELD PL MEASUREMENT

A unique and state of art equipment is used in this work, which is the wide-field PL. This equipment can take the PL intensity, transmittance (TR), Photoconductivity (PC), and the degradation video simultaneously. Moreover, with some effort, it can take the dark field image at the same time as well. Wide-field absolute intensity PL measurements were conducted with a Hamamatsu C11440 camera with a Lumencor SpectraX light source and Mitutoyo 100x objective. The darkfield image is taken by Olympus MPLFLN50XBD. A green LED is used for excitation, which is then filtered with a 32 nm wide-band-pass filter centered at 560 nm. The excitation source is passed through a filter cube with a dichroic mirror and an emission long-pass filter to achieve a minimum OD 8 suppression for excitation wavelengths. And the RH is controlled by filtering the gas through glycerol water mixed solution[46].

3.3.1 *Photoluminescence Video Analysis (PLVA)*

For MAPbI3 composition, both spin-coated and pre-scored-spray coated sample is used in this experiment. The spray-coated sample is broken into 15 * 15 mm pieces and measured at the same condition with the spin-coated sample. Temperature is controlled by hotplate and the sample is exposed in ambient condition with 16Sun intensity. And for CsPbI3 composition, the sample is sealed in closed stage (Linkam Scientific LTSE420-P) and filled with 60% RH Air and 8Sun intensity. The sample is continuously illuminated and heated through the whole experiment and data is collected every minute repeatedly.

3.3.2 *PL-PC-TR Measurement*

$MAPbI_3$ films are tested by using PL-PC-TR measurement. The substrates are evaporated with 80nm thick Au contact. And Photoconductivity was measured by connecting Au contacts to a

Keithley 2400 source measurement unit and sourcing + or – 3V while measuring current. A photodiode is connected to another Keithley 2400 and put under the Linkam stage with a maximum current shown on the Keithley at initial stage. The frequency of illumination is controlled by a waveform generator (Agilent 33500B). The LED intensity and time interval between each measurement is controlled by python and micromanager. And the gas flow through the stage is constant at 2L/min.

3.4 XRD MEASUREMENT

XRD is commonly used to determine the structure of a material. In this work, XRD is used to characterize the phase of $CsPbI_3$ since different phases could form during the fabrication. The 2-theta scan is from 10 degrees to 65 degrees with 0.3mm collimator and 6100 thresholds. The equipment model is Bruker D8 Discover Microfocus.

3.5 DEGRADATION SIMULATION

The $MAPbI_3$ degradation mechanism simulation is using python language. The 3D degradation problem can be simplified into a 2D diffusion problem plus evaporation of organic gases. By assuming the evaporation rate is proportional to the concentration, the function for evaporation can be written as

$$u_{i,j}^{(n+1)\prime} = \Delta t k_{evap} u_{i,j}^{(n)} \tag{3.1}$$

where $u_{i,j}^{(n+1)\prime}$ indicates the evaporated concentration, k_{evap} is the evaporation coefficient. Combine this equation with equation 2.9, the final degradation function can be achieved as below,

$$u_{i,j}^{(n+1)} = D\Delta \mathrm{t}\left(\frac{u_{i+1,j}^{(n)} - 2u_{i,j}^{(n)} + u_{i-1,j}^{(n)}}{(\Delta x)^2} + \frac{u_{i,j+1}^{(n)} - 2u_{i,j}^{(n)} + u_{i,j-1}^{(n)}}{(\Delta y)^2}\right) + (1 - \Delta t k_{evap}) u_{i,j}^{(n)} \tag{3.2}$$

A 1000 * 1000 matrix with initial value 1 is built, and the defect region are randomly created, which has the initial value 0. By applying the equation 3.2 with each pixel except the edges for 1000 times and save every calculated matrix in a list with order. Finally, the degradation simulation animation can be generated by converting the list.

Chapter 4. RESULT AND DISCUSSION

4.1 FILM CHARACTERIZATION

4.1.1 *UV-Vis Result*

The spin coated $MAPbI_3$ and FACs composition films are tested. The Tauc plot is shown in Figure 4.1.

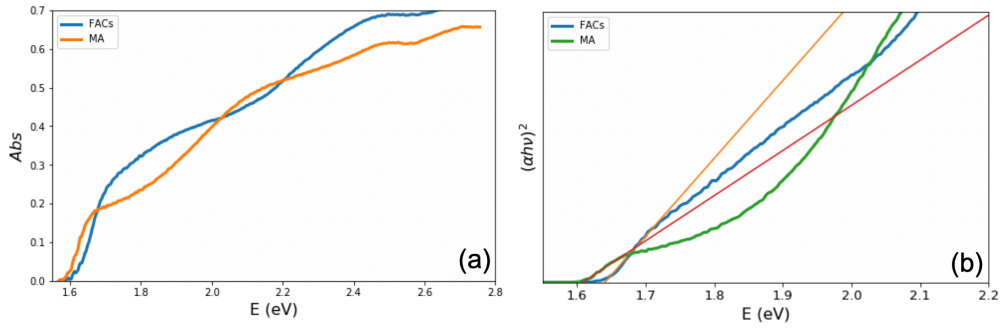

Figure 4.1 (a)UV-Vis absorbance plot and (b)Tauc plot for the two substrates.

In the Tauc. plot method[47,48], equation 3.3 is applied. To plot the $(\alpha h\upsilon)^2$ against E_g with the equation below:

$$(\alpha h\upsilon)^2 = A(h\upsilon - \mathrm{E}_g) \tag{4.1}$$

In this equation, α is absorption coefficient, h is plank's constant, υ is frequency, A is proportionality constant, and E_g is the bandgap. By applying the equation, the bandgap is the interception of the tangent line. The bandgap of two materials are 1.61eV for $MAPbI_3$ and 1.64eV for $(FA_{.87}Cs_{.13})Pb(I_{.86}Br_{.14})_3$ based on the plot.

4.1.2 *XRD Results*

There are several phases can be formed through the fabrication of $CsPbI_3$. Therefore, it is important to make sure the fabricated $CsPbI_3$ is perovskite phase, which are cubic or orthorhombic phase.

The $CsPbI_3$ substrates are taken to do the XRD measurement in order to figure it out. The result is shown in Figure 4.2.

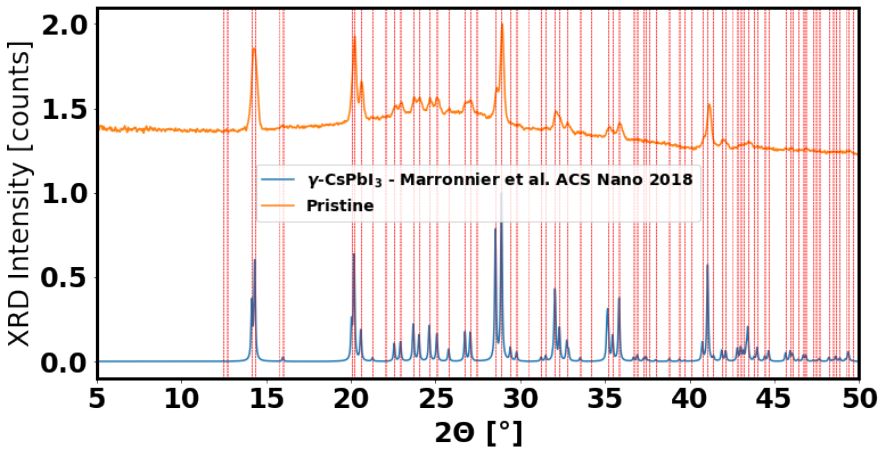

Figure 4.2 XRD Patterns for $CsPbI_3$

Compared with reference[49], each peak is paired very well. Therefore, the black film fabricated by the previous method is the orthorhombic phase, which is believed to be a perovskite phase with the bandgap of 1.73eV.

4.2 Degradation Video Results

4.2.1 *Spin and Spray Coated $MAPbI_3$ Substrates*

The PL video is taken for both materials. The plot for PLQY vs. Time is shown in Figure 4.3(a). For both substrates' PL videos, four images of each are extracted from the video: time zero, at 1/3, 2/3 and fully degraded as shown in Figure 4.3(b) and (c). The sprayed sample has a higher PLQY and longer lifetime. This may due to the different defect concentration and fabrication method for each substrate. From Figure 4.3(c), the spin-coated sample degrades very fast and uniformly. In contrast, the spray-coated sample starts with some small domains, which believed to be a big defect from manufacturing, and have the highest PL at the beginning. Then the film starts photo-brightening, and the defect domain starts growing with photo dimming, eventually cross the whole

area. The two different degradation patterns are believed due to the different defects' density and size of pinhole, which comes from the different fabrication methods since the experiment conditions are remain the same.

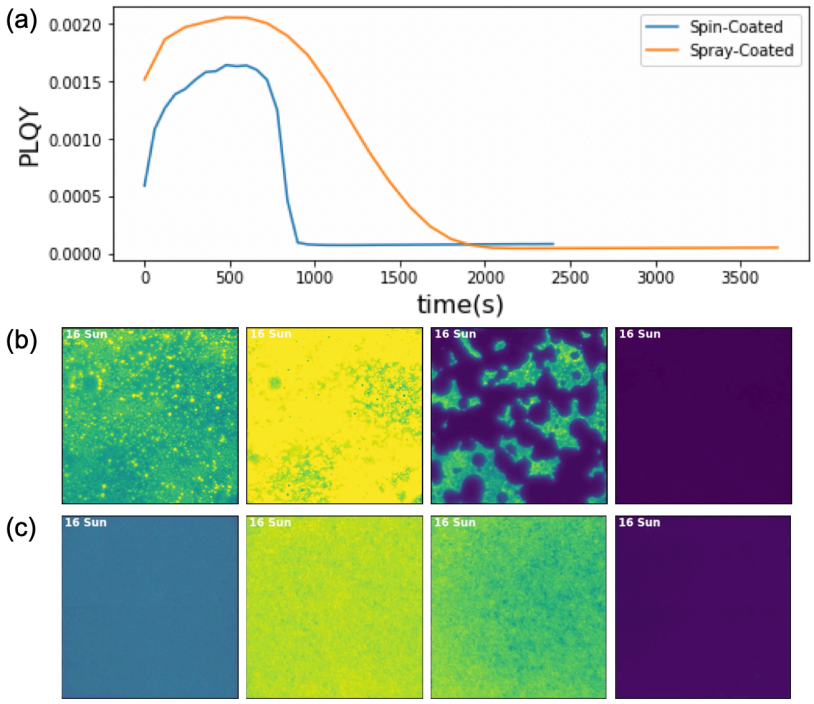

Figure 4.3 (a)PLQY vs. t, and screenshots of the degradation videos for (b)spray-coated film and (c)spin-coated film

The peer result shows that the spray-coated sample here has more pinholes and less uniformed film. And the post degradation film is much more transparent than before at the illumination area. A hypothesis has been made that the degradation is due to a mass loss mechanism, and it starts more easily from the weak domain, such as defects. The $MAPbI_3$ will be decomposed into MAI and PbI_2 when the degradation happens under this condition. And then, the MAI will be evaporated from the surface and left PbI_2, which will not photoluminescence under green LED illumination. To further investigate that the degradation starts from the weak area, the prescribed sample is prepared. The deliberately introduced defect is at the top right corner of the frame, and the whole

film is under the same condition as the previous experiment. The degradation video's frames are shown in Figure 4.4. Just like proposed, the degradation starts around the defects and then quickly spread to the whole area. Which is highly support the hypothesis. After the experiment, the illuminated area becomes transparent. This bleaching phenomenon is believed due the formation of PbI_2. The outside region is slightly pale than before, but not obvious.

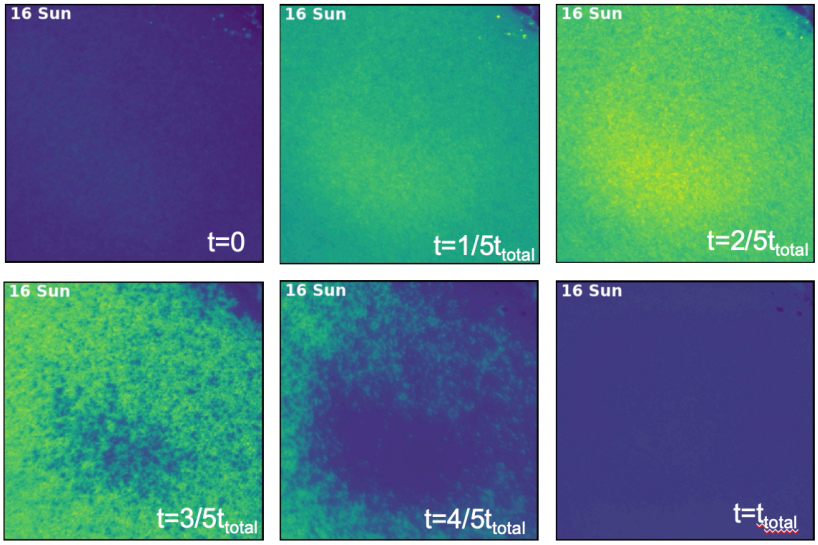

Figure 4.4 The PLQY video screenshots at six time spots on the pre-scribed sample

Based on the previous experiment results, a hypothesis is that the film degradation is go through a mass loss mechanism, and the proposed degradation mechanism is shown in Figure 4.5

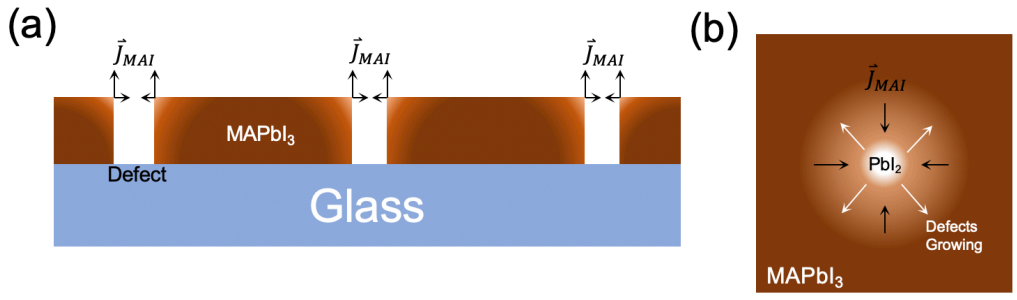

Figure 4.5 The potential degradation mechanism for $MAPbI_3$, (a)front view of the film, and (b)top view of a defect domain

In Figure 4.5, the brown area is the $MAPbI_3$ perovskite phase and the blank area are defects, such as pinhole or non-perovskite phase, the PbI_2, and the area in pale brown are the degrading area where the $MAPbI_3$ will decompose into MAI and PbI_2. The generated MAI will either be evaporated from the film or diffuse into the defect region, where have low concentration of MAI. And this diffusion and evaporation behavior is shown in black arrow. And the white arrow in Figure 4.5(b) indicates the expansion of bleaching area, also known as defect region.

4.2.2 *$CsPbI_3$ PL Video Results*

The degradation mechanism of the $CsPbI_3$ sample is phase transition, from perovskite phase to non-perovskite α phase. The $CsPbI_3$ PL video is taken as well to suggest that this $MAPbI_3$ degradation is not follow the same path. Similarly, the four extracted frames for QFLS degradation video are shown in Figure 4.6(a). The degradation patterns are very different from the $MAPbI_3$ sample. The film starts photo brightening as well but not uniformly. Then some of the region start losing PL but the adjacent domains are not. Even the film become transparent, the film still has some PL, like shown in the Figure 4.6(a). This may due to the remaining not degraded perovskite phase. This result suggested that $MAPbI_3$ degradation is not the phase transition mode. Similarly, to test out whether the defect has the same effect on the degradation, a prescribed sample has been made as well. The camera is also focused on the defect area. The separated frames for the QFLS degradation video are shown in Figure 4.6(b). The result is not like the $MAPbI_3$ substrate and have similar behavior with the un-scribed substrate. In the video, the defect region is not growing, and the other region is photo brightening and diming as the un-scribed one does.

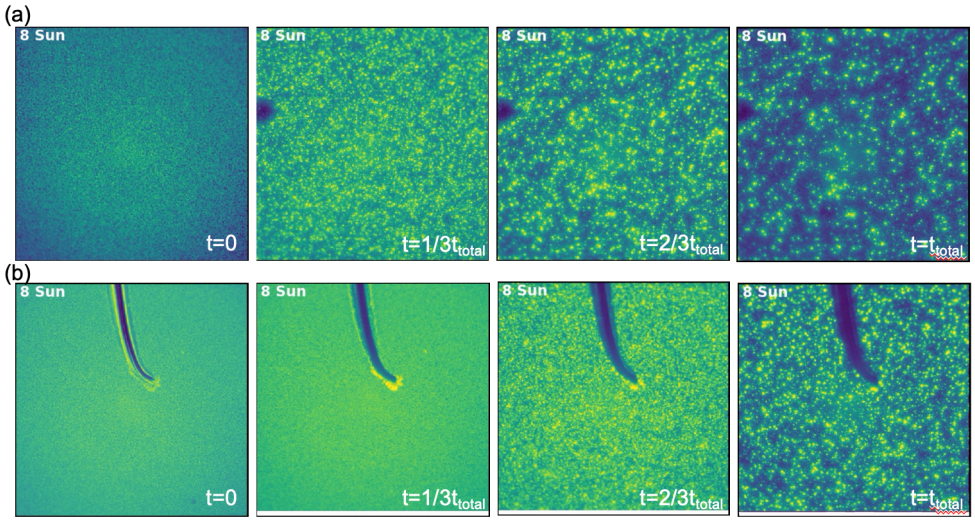

Figure 4.6 The QFLS degradation video frames on the (a)pristine, and (b)pre-scribed $CsPbI_3$ sample

4.3 PL-PC-TR RESULTS

To explore the influence among environmental factors and film degradation, 27 experiments were designed and analyzed. There are three level of oxygen percentage, five level of RH, four level of temperature and two level of excitation Intensity in total. The environment conditions for them are shown in Table 4.1. In these experiments, 0% oxygen means pure N_2, and 21% oxygen is air. In these experiments, the diffusion length, transmissivity and PLQY are collected and calculated, then normalized twice. At first, the data is collected and then normalized with itself. Then all the 27 normalized data is put together and normalized again. This is for an easier comparison and analyzing. Otherwise the transmittance will dramatically change from 8 to 300 under different sun intensity for example. First, to analyze how the sample behave under low excitation intensity and

Table 4.1 Designed Experiments for $MAPbI_3$ degradation study

Experiments No.	Oxygen Percentage	Relative Humidity	Temperature	Excitation Intensity
1	21	0	85	32
2	21	20	85	32
3	21	40	85	32
4	21	60	85	32
5	21	80	85	32
6	21	0	25	8
7	21	20	25	8
8	21	40	25	8
9	21	60	25	8
10	21	80	25	8
11	21	60	45	8
12	21	60	65	8
13	21	60	85	8
14	0	0	25	8
15	0	60	25	8
16	100	60	85	32
17	21	60	85	32
18	100	20	85	32
19	100	60	25	32
20	21	60	25	32
21	100	20	25	32
22	21	20	25	32
23	100	60	85	8
24	100	20	85	8
25	21	20	85	8
26	100	60	25	8
27	100	20	25	8

low temperature with different level of gas environment, six experiments' results are compared (Experiment No.6, 9, 14, 15, 26, 27), and shown in Figure 4.7. In the dry N_2 case, the transmittance only increased 0.0012, and the diffusion length is also not decreasing in 200 minutes, which indicates the film is not changing at all. Since the formation of PbI_2 will bleach the film and increasing the transmittance dramatically, like other experiments. And by increasing the RH to 60%, the film starts to degrade in the first 200 minutes and have a final transmittance at around

0.66. The film degradation is accelerated by increasing the oxygen percentage. In low RH cases, the film lifetime is shortened from super long to only 150 minutes in pure oxygen. Similarly, the transmittance will reach about 0.6 within 1 hour in 60RH pure oxygen case, which is much faster than the pure N_2 case. These six experiments are very important since it give a base line for the whole experiment, like not degraded as for dry N_2 case and fully degraded for 60RH air cases. Interestingly, the RH seems have a huge influence on the degradation speed, as well as oxygen. This result shows a great agreement on the current theory that humidity and oxygen are two of the main factors that affect the film stability.

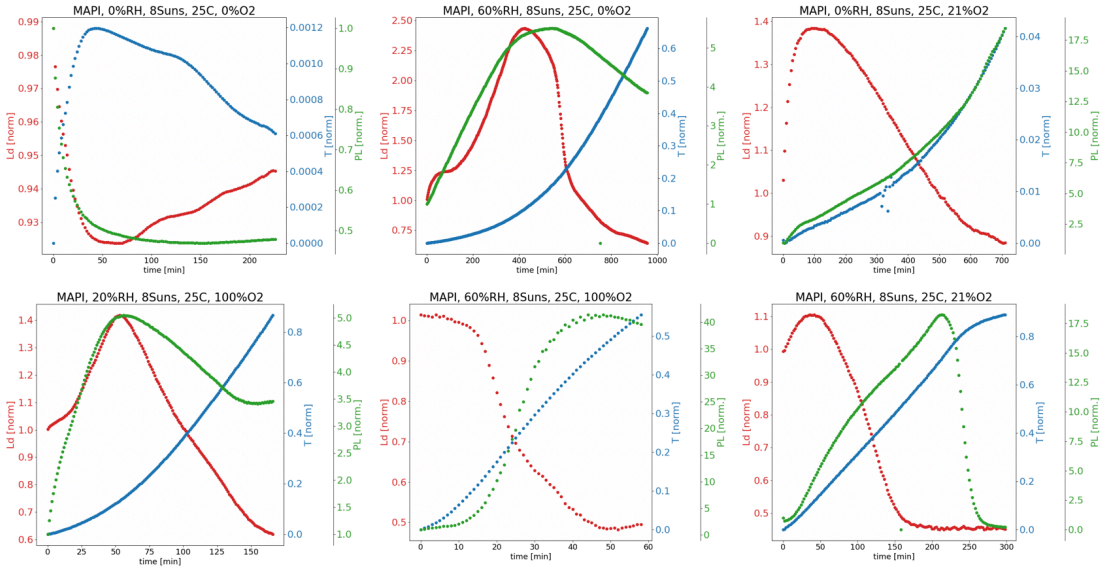

Figure 4.7 Normalized diffusion length, transmissivity, and PLQY data for $MAPbI_3$ Experiment No. 6, 9, 14, 15, 26, 27

Then take all the cases that under low excitation intensity but at high RH in air (Experiment No.9, 11, 12, 13, 23, 26) as a group to explore how the temperature and oxygen can affect. It is obvious that the film lifetime is decreasing with the increasing of temperature. For the cases have temperature lager than 25C, the transmittance all driven to 1 at last. And the time needed is shorten from 600 minutes to 120 minutes, even up to about 30 minutes with higher oxygen percentage.

This indicates that the temperature accelerates the degradation very much. And interestingly, the highest PLQY is decreasing with the increased temperature.

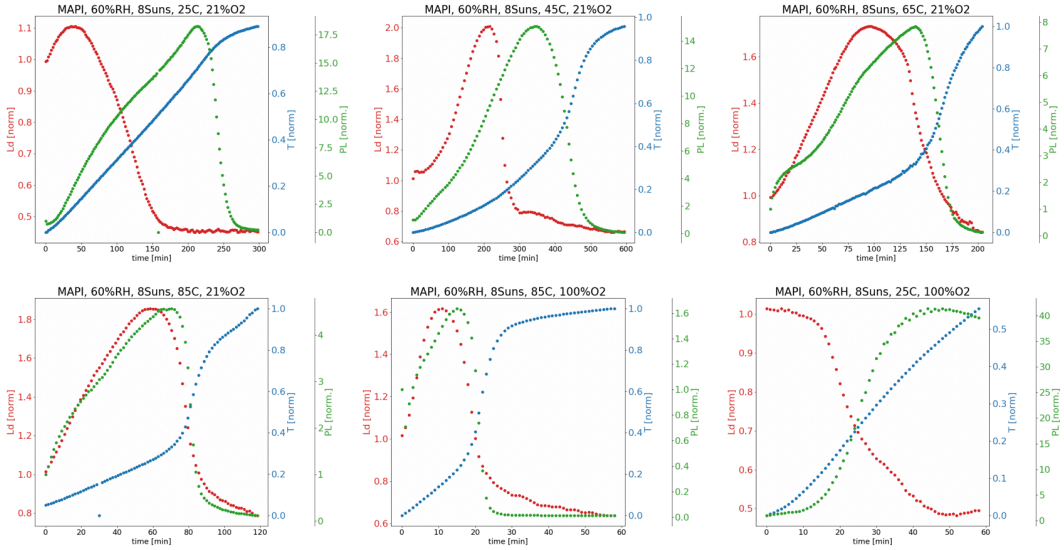

Figure 4.8 Normalized diffusion length, transmissivity, and PLQY data for $MAPbI_3$ Experiment No. 9, 11, 12, 13, 23, 26

Then the high sun intensity and thermal stress runs are grouped (Experiment No.1, 2, 3, 4, 5, 16, 17, 18) and shown in Figure 4.9. Overall the lifetime of films are within 60 minutes, which is far less than the ones in low stress cases. However, the behavior is less regulated for these high stress cases. All the films in air seem have multi photo brightening stages. This means that the film is photo brightening at the beginning, and then photo dimming. But then, it will photo brightening and diming again before fully degraded. And for the unusual behavior of 60RH 21% oxygen run, the increased PL at the end of the run is current unexplainable.

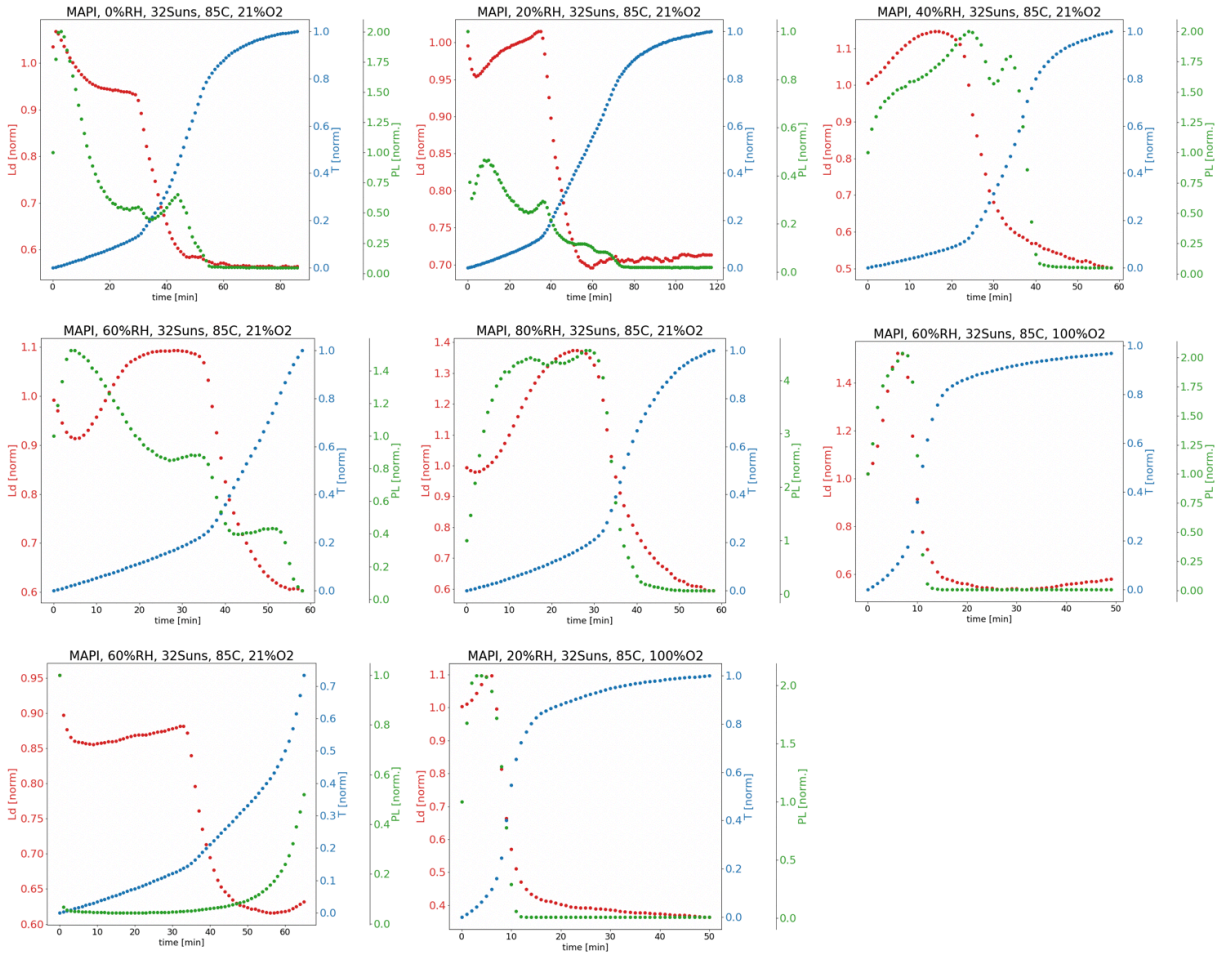

Figure 4.9 Normalized diffusion length, transmissivity, and PLQY data for $MAPbI_3$ Experiment No.1, 2, 3, 4, 5, 16, 17, 18

And finally, take 8suns, 25C in air cases (Experiment No.6, 7, 8, 9, 10) as a group. The results are shown in Figure 4.10. Lifetime still follows the previous result that the film is more and more unstable with the increasing of RH. But unlike the high temperature runs, PL increased significantly with the increased RH. To figure it out, several darkfield images are shown in Figure 4.11.

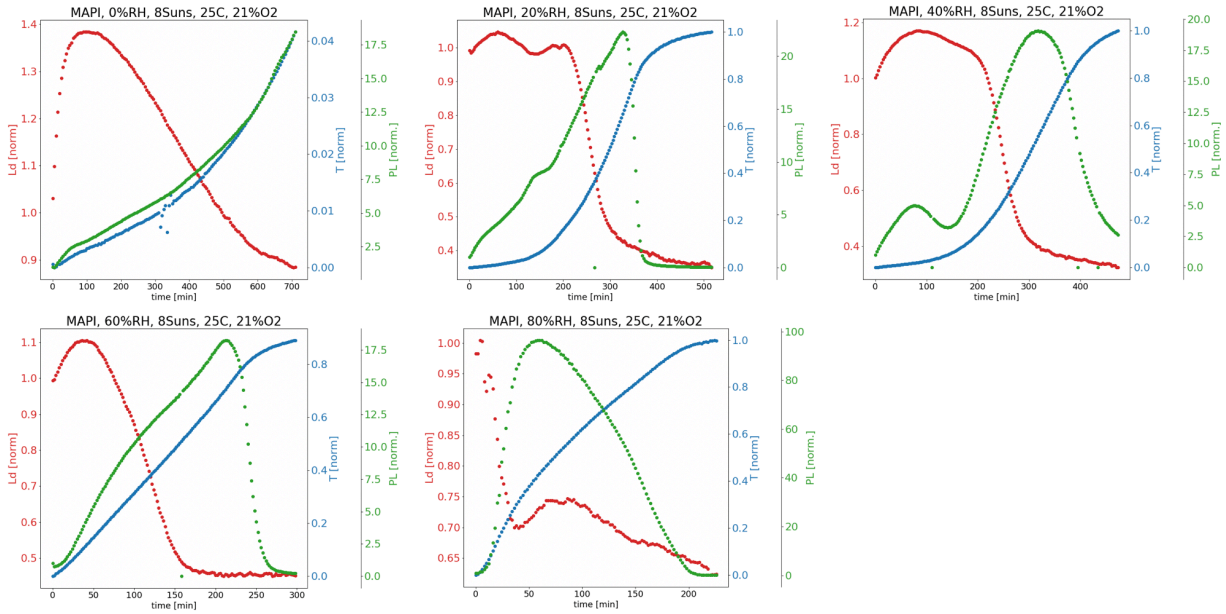

Figure 4.10 Normalized diffusion length, transmissivity, and PLQY data for $MAPbI_3$ Experiment No.6, 7, 8, 9, 10

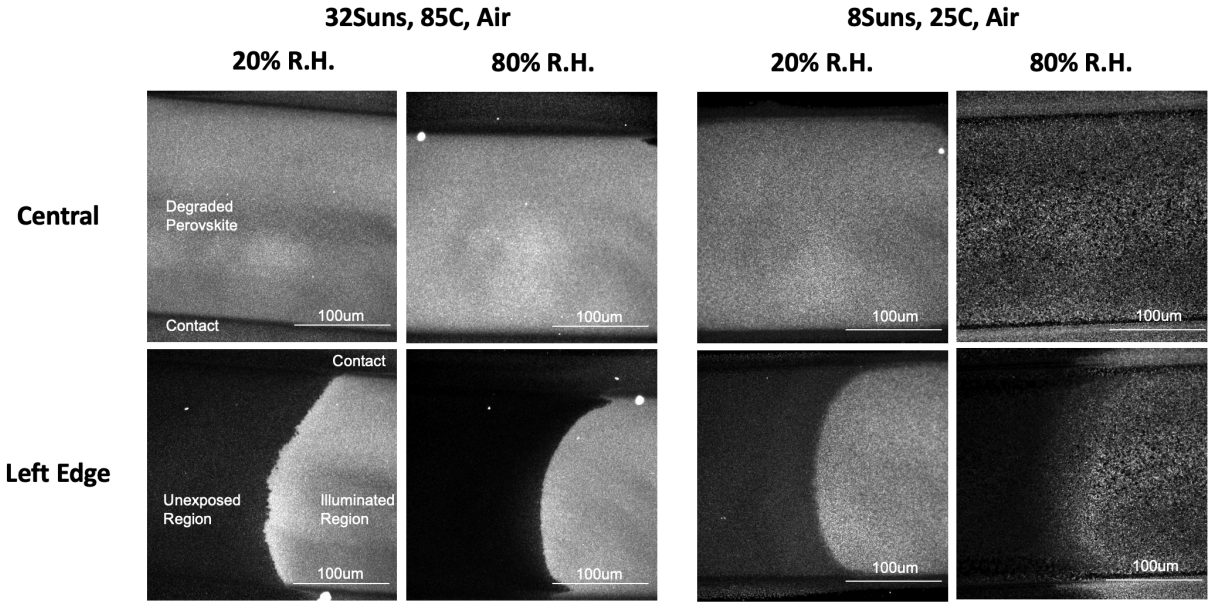

Figure 4.11 Post degradation darkfield image for Experiment No.2, 5, 7, 10

These darkfield images are the post degradation darkfield images from Experiment No.2, 5, 7, and 10. In these figures, the upper and bottom part are the gold contact, and the middle region is the

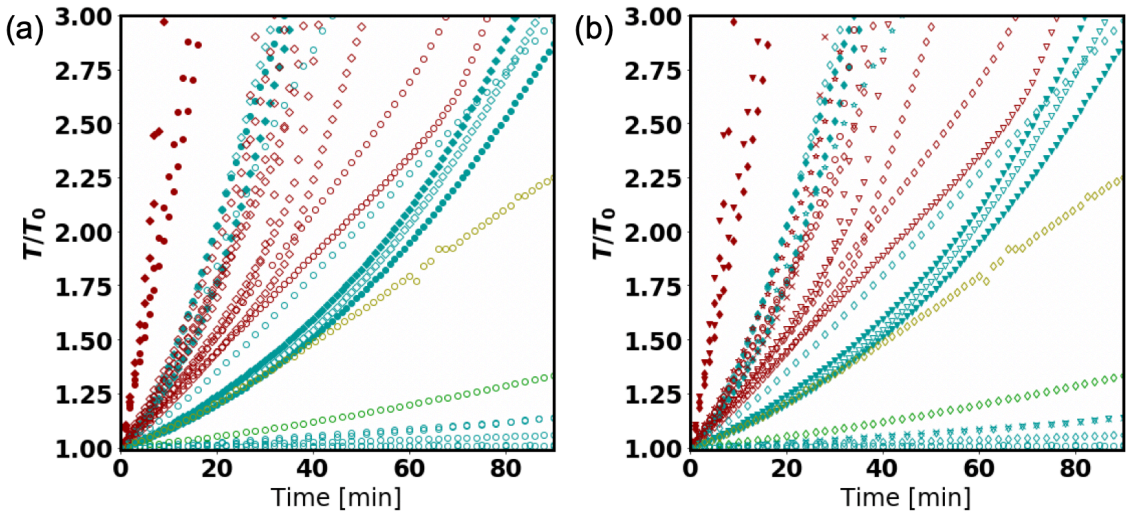

Figure 4.12 First 90 min transmittance data grouped by (a) temperature(cyan for 25C, green for 45C, yellow for 65C, and red for 85C), illumination intensity(circle for 8suns, diamond for 32suns), and oxygen(unfilled for less than 50%, filled for pure oxygen); (b) temperature(cyan for 25C, green for 45C, yellow for 65C, and red for 85C), relative humidity(circle for 0RH, triangle for 20RH, x for 40RH, diamond for 60RH, and star for 80RH) and oxygen(unfilled for less than 50%, filled for pure oxygen)

exposed perovskite film. For the first row is the central region of illuminated area, and the second row is the area slightly to the left edge, which contains the directly illuminated region, which is relative brighter, and unexposed region, which is the dark region. For the high stressed runs, the edge of two region is clear and there is not much feature in those two regions. However, in the low stressed cases, the edge is becoming less obvious with the increasing of RH. In 20RH run, the edge is less sharp, and the surface is apparently rougher. In 80RH case, it becomes a gradient from center to the edge. And there are a lot of needle liked defects, which is not shown in high stress cases. These needle liked defects may be the hydrated perovskite or post degradation chemicals, since they only appear in low temperature runs. Because the hydrated phenomenon is reversible

by heating the substrate, which means at high temperature the hydrated compounds are less likely to form.

Table 4.2 Real experiment condition and calculated results

Experiment No.	Temperature	Relative Humidity	Oxygen Percentage	Excitation Intensity	Bleaching Rate	PL Max
1	85	0	21	32	0.0314136	0.00018137
2	85	24.8	21	32	0.0220687	0.00020042
3	85	39.5	21	32	0.0294375	0.00014521
4	85	59.3	21	32	0.0328584	0.00018974
5	85	80.6	21	32	0.0366656	0.00028272
6	25	0	21	8	6.965E-05	0.0023475
7	25	25.7	21	8	0.0009099	0.01395451
8	25	45.8	21	8	0.0013177	0.00914969
9	25	59.5	21	8	0.015877	0.00385111
10	25	80.5	21	8	0.0283072	0.0572411
11	45	60	21	8	0.0024679	0.00520483
12	65	54.3	21	8	0.0084383	0.00148408
13	85	55.1	21	8	0.0226451	0.00035197
14	25	0	0	8	0.0005891	0.00034184
15	25	57.9	0	8	0.0008408	0.00817411
16	85	61.9	100	32	0.1235446	0.000875
17	85	61.9	21	32	0.0187151	0.00014756
18	85	24.4	100	32	0.1428417	0.0013221
19	25	58.1	100	32	0.0260615	0.01279816
20	25	57	21	32	0.0321537	0.01822569
21	25	18.7	100	32	0.0081707	0.01034982
22	25	18.7	21	32	0.0076593	0.01083766
23	85	62.7	100	8	0.0998	0.00087468
24	85	21.6	100	8	0.1096776	0.00098591
25	85	25.1	21	8	0.0217294	0.00033517
26	25	62.4	100	8	0.0268144	0.02773501
27	25	24	100	8	0.006908	0.0046992

At last, all the calculated bleaching rate, which is the fitted slope of the first five points from transmittance line, is shown in Table 4.2. As shown in the table, the RH is replaced with the real RH during the experiments, and the PL max is the highest PLQY the film can reach. It is not

surprising that the highest bleaching rate comes from the high temperature, high illumination and pure oxygen runs, but the humidity seems suppress the bleaching rate at high stress a little. For a better visualization of the bleaching rate, the first 90 minutes variance of transmittance are shown in Figure 4.12. The overall trend can be found from these two figures. As described previously, the temperature has a dominant influence on the bleaching rate, most of the high temperature runs have a relative higher bleaching rate than the low temperature runs. For the low temperature runs, the impact from oxygen and illumination is less than humidity. However, the oxygen has more impact at high temperature.

4.4 DEGRADATION SIMULATION

By applying the real-world physical law, a degradation animation is generated, as described in the previous section. And a couple of the frames are shown in Figure 4.13

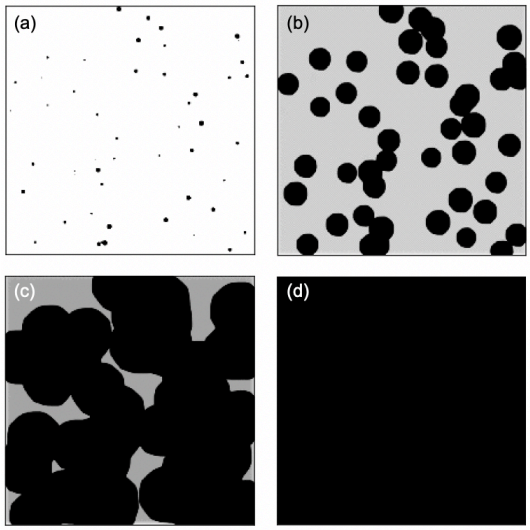

Figure 4.13 Extracted frames from the degradation simulation video at (a)t = 0, (b)t = $1/3t_{total}$, (c)t=$2/3\ t_{total}$, and (d)t= t_{total}.

As shown in the figure, at the very beginning, the defect region is very small, and the frame is mostly bright, which here is dominated by $MAPbI_3$. Then the defect region, black area, starts to

grow and the whole frame is getting grayer. The color from white to black is the concentration from 1M to 0. This indicates that the diffusion and evaporation process is happening. As time flows, MAI continuously diffuses into the PbI_2 domain and the organic part evaporating from the film at the same time, leading the defect region to become bigger, and other regions become darker. At last, the whole frame is occupied by the black area, and this indicates that the film is fully degraded. The results show significant similarity with the degradation frames shown in Figure 4.3(b). This result highly supports the degradation hypothesis that $MAPbI_3$ degradation is a mass loss process.

Chapter 5. CONCLUSION AND FUTURE WORK

In this work, we have introduced a state of art degradation measurement technology that can control the environment, take the degradation video, and measure PLQY, diffusion length, and transmittance at the same time. Firstly, by using this equipment, we have taken several degradation videos of $MAPbI_3$ and $CsPbI_3$ compositions for both pristine sample and pre-scribed samples. And by observing the degradation video, we noticed that the $MAPbI_3$ sample does not follow the phase transition degradation, which is the $CsPbI_3$ degradation pathway. We applied a diffusion and evaporation simulation by python have a good agreement with the correctness of our previous hypothesis and proved the reliability of our results comes from the equipment. We also developed a highly reproducible fabrication method for the compositions that have been mentioned previously.

In addition, we revealed the influence and relationship among RH, temperature, excitation intensity, and oxygen percentage during degradation. For $MAPbI_3$ composition, humidity is less important in high-stress cases and will significantly impact the PL in low-stress cases. Illumination would also accelerate the degradation at high temperatures as well as low oxygen cases. We also find that the degradation rate changes when diffusion length starts failing in most cases. This result is very necessary for future works. And most importantly, we discovered a new, easily measurable data other than the QFLS and PLQY, the transmittance in quantifying the degradation process. And the fitted slope of the transmittance data, which we called bleaching rate, is also a very important parameter to demonstrate the degradation process. This parameter can be used in predicting the lifetime of perovskite, which has a significant contribution in the perovskite research area. And we also find that the humidity can suppress the bleaching rate in high stress cases.

For future study, the effect of different environmental stresses will be continuously investigated, not only a more sophisticate conditions but also tested on more compositions, such as FACs composition mentioned in this paper, 2D perovskite and even triple cation perovskite films. It is necessary to dig into the FACs composition perovskite degradation mechanism investigation in the future as well, since it shows great stability and performance in this field. And for the simulation results, it still under developing, since the parameter is not directly measured from the degradation experiment. And as we show in this paper, at high humidity cases the degradation mechanism contains hydration, which is not include in the simulation yet.

REFERENCES.

(1) Kojima, A.; Teshima, K.; Shirai, Y.; Miyasaka, T. Organometal Halide Perovskites as Visible-Light Sensitizers for Photovoltaic Cells. *J. Am. Chem. Soc.* **2009**, *131* (17), 6050–6051. https://doi.org/10.1021/ja809598r.

(2) Mazzarella, L.; Lin, Y. H.; Kirner, S.; Morales-Vilches, A. B.; Korte, L.; Albrecht, S.; Crossland, E.; Stannowski, B.; Case, C.; Snaith, H. J.; et al. Infrared Light Management Using a Nanocrystalline Silicon Oxide Interlayer in Monolithic Perovskite/Silicon Heterojunction Tandem Solar Cells with Efficiency above 25%. *Adv. Energy Mater.* **2019**, *9* (14), 1–9. https://doi.org/10.1002/aenm.201803241.

(3) Green, M. A.; Ho-Baillie, A.; Snaith, H. J. The Emergence of Perovskite Solar Cells. *Nat. Photonics* **2014**, *8* (7), 506–514. https://doi.org/10.1038/nphoton.2014.134.

(4) Li, C.; Lu, X.; Ding, W.; Feng, L.; Gao, Y.; Guo, Z. Formability of ABX 3 (X = F, Cl, Br, I) Halide Perovskites. *Acta Crystallogr. Sect. B Struct. Sci.* **2008**, *64* (6), 702–707. https://doi.org/10.1107/S0108768108032734.

(5) Umari, P.; Mosconi, E.; De Angelis, F. Relativistic GW Calculations on CH3 NH3 PbI 3 and CH3 NH3 SnI3 Perovskites for Solar Cell Applications. *Sci. Rep.* **2014**, *4*, 1–7. https://doi.org/10.1038/srep04467.

(6) Kieslich, G.; Sun, S.; Cheetham, A. K. Solid-State Principles Applied to Organic–Inorganic Perovskites: New Tricks for an Old Dog. *Chem. Sci.* **2014**, *5* (12), 4712–4715. https://doi.org/10.1039/c4sc02211d.

(7) Cheng, Z.; Lin, J. Layered Organic-Inorganic Hybrid Perovskites: Structure, Optical Properties, Film Preparation, Patterning and Templating Engineering. *CrystEngComm* **2010**, *12* (10), 2646–2662. https://doi.org/10.1039/c001929a.

(8) Umebayashi, T.; Asai, K.; Umebayashi, T.; Asai, K.; Kondo, T.; Kondo, T.; Nakao, A. Electronic Structures of Lead Iodide Based Low-Dimensional Crystals. *Phys. Rev. B - Condens. Matter Mater. Phys.* **2003**, *67* (15), 2–7. https://doi.org/10.1103/PhysRevB.67.155405.

(9) Protesescu, L.; Yakunin, S.; Bodnarchuk, M. I.; Krieg, F.; Caputo, R.; Hendon, C. H.; Yang, R. X.; Walsh, A.; Kovalenko, M. V. Nanocrystals of Cesium Lead Halide Perovskites (CsPbX3, X = Cl, Br, and I): Novel Optoelectronic Materials Showing Bright Emission with Wide Color Gamut. *Nano Lett.* **2015**, *15* (6), 3692–3696. https://doi.org/10.1021/nl5048779.

(10) Yang, Z.; Chueh, C. C.; Liang, P. W.; Crump, M.; Lin, F.; Zhu, Z.; Jen, A. K. Y. Effects of Formamidinium and Bromide Ion Substitution in Methylammonium Lead Triiodide

toward High-Performance Perovskite Solar Cells. *Nano Energy* **2016**, *22*, 328–337. https://doi.org/10.1016/j.nanoen.2016.02.033.

(11) Saidaminov, M. I.; Abdelhady, A. L.; Murali, B.; Alarousu, E.; Burlakov, V. M.; Peng, W.; Dursun, I.; Wang, L.; He, Y.; MacUlan, G.; et al. High-Quality Bulk Hybrid Perovskite Single Crystals within Minutes by Inverse Temperature Crystallization. *Nat. Commun.* **2015**, *6* (May), 1–6. https://doi.org/10.1038/ncomms8586.

(12) Leijtens, T.; Bush, K.; Cheacharoen, R.; Beal, R.; Bowring, A.; McGehee, M. D. Towards Enabling Stable Lead Halide Perovskite Solar Cells; Interplay between Structural, Environmental, and Thermal Stability. *J. Mater. Chem. A* **2017**, *5* (23), 11483–11500. https://doi.org/10.1039/c7ta00434f.

(13) Cheacharoen, R.; Boyd, C. C.; Burkhard, G. F.; Leijtens, T.; Raiford, J. A.; Bush, K. A.; Bent, S. F.; McGehee, M. D. Encapsulating Perovskite Solar Cells to Withstand Damp Heat and Thermal Cycling. *Sustain. Energy Fuels* **2018**, *2* (11), 2398–2406. https://doi.org/10.1039/c8se00250a.

(14) Leguy, A. M. A.; Hu, Y.; Campoy-Quiles, M.; Alonso, M. I.; Weber, O. J.; Azarhoosh, P.; Van Schilfgaarde, M.; Weller, M. T.; Bein, T.; Nelson, J.; et al. Reversible Hydration of CH3NH3PbI3 in Films, Single Crystals, and Solar Cells. *Chem. Mater.* **2015**, *27* (9), 3397–3407. https://doi.org/10.1021/acs.chemmater.5b00660.

(15) Yang, J.; Siempelkamp, B. D.; Liu, D.; Kelly, T. L. Investigation of CH3NH3PbI3degradation Rates and Mechanisms in Controlled Humidity Environments Using in Situ Techniques. *ACS Nano* **2015**, *9* (2), 1955–1963. https://doi.org/10.1021/nn506864k.

(16) Christians, J. A.; Miranda Herrera, P. A.; Kamat, P. V. Transformation of the Excited State and Photovoltaic Efficiency of CH3NH3PbI3 Perovskite upon Controlled Exposure to Humidified Air. *J. Am. Chem. Soc.* **2015**, *137* (4), 1530–1538. https://doi.org/10.1021/ja511132a.

(17) Li, Y.; Xu, X.; Wang, C.; Wang, C.; Xie, F.; Yang, J.; Gao, Y. Degradation by Exposure of Coevaporated CH3NH3PbI3 Thin Films. *J. Phys. Chem. C* **2015**, *119* (42), 23996–24002. https://doi.org/10.1021/acs.jpcc.5b07676.

(18) Ruess, R.; Benfer, F.; Böcher, F.; Stumpp, M.; Schlettwein, D. Stabilization of Organic-Inorganic Perovskite Layers by Partial Substitution of Iodide by Bromide in Methylammonium Lead Iodide. *ChemPhysChem* **2016**, *17* (10), 1505–1511. https://doi.org/10.1002/cphc.201501168.

(19) Alberti, A.; Deretzis, I.; Pellegrino, G.; Bongiorno, C.; Smecca, E.; Mannino, G.; Giannazzo, F.; Condorelli, G. G.; Sakai, N.; Miyasaka, T.; et al. Similar Structural Dynamics for the Degradation of CH 3 NH 3 PbI 3 in Air and in Vacuum. *ChemPhysChem* **2015**, *16* (14), 3064–3071. https://doi.org/10.1002/cphc.201500374.

(20) Zhao, J.; Cai, B.; Luo, Z.; Dong, Y.; Zhang, Y.; Xu, H.; Hong, B.; Yang, Y.; Li, L.; Zhang, W.; et al. Investigation of the Hydrolysis of Perovskite Organometallic Halide CH3NH3PbI3 in Humidity Environment. *Sci. Rep.* **2016**, *6* (December 2015), 1–6. https://doi.org/10.1038/srep21976.

(21) Yang, B.; Dyck, O.; Ming, W.; Du, M. H.; Das, S.; Rouleau, C. M.; Duscher, G.; Geohegan, D. B.; Xiao, K. Observation of Nanoscale Morphological and Structural Degradation in Perovskite Solar Cells by in Situ TEM. *ACS Appl. Mater. Interfaces* **2016**, *8* (47), 32333–32340. https://doi.org/10.1021/acsami.6b11341.

(22) Charles, B.; Dillon, J.; Weber, O. J.; Islam, M. S.; Weller, M. T. Understanding the Stability of Mixed A-Cation Lead Iodide Perovskites. *J. Mater. Chem. A* **2017**, *5* (43), 22495–22499. https://doi.org/10.1039/c7ta08617b.

(23) Juarez-Perez, E. J.; Hawash, Z.; Raga, S. R.; Ono, L. K.; Qi, Y. Thermal Degradation of CH3NH3PbI3 Perovskite into NH3 and CH3I Gases Observed by Coupled Thermogravimetry-Mass Spectrometry Analysis. *Energy Environ. Sci.* **2016**, *9* (11), 3406–3410. https://doi.org/10.1039/c6ee02016j.

(24) Conings, B.; Drijkoningen, J.; Gauquelin, N.; Babayigit, A.; D'Haen, J.; D'Olieslaeger, L.; Ethirajan, A.; Verbeeck, J.; Manca, J.; Mosconi, E.; et al. Intrinsic Thermal Instability of Methylammonium Lead Trihalide Perovskite. *Adv. Energy Mater.* **2015**, *5* (15), 1–8. https://doi.org/10.1002/aenm.201500477.

(25) Han, Q.; Bae, S. H.; Sun, P.; Hsieh, Y. T.; Yang, Y.; Rim, Y. S.; Zhao, H.; Chen, Q.; Shi, W.; Li, G.; et al. Single Crystal Formamidinium Lead Iodide (FAPbI3): Insight into the Structural, Optical, and Electrical Properties. *Adv. Mater.* **2016**, *28* (11), 2253–2258. https://doi.org/10.1002/adma.201505002.

(26) Binek, A.; Hanusch, F. C.; Docampo, P.; Bein, T. Stabilization of the Trigonal High-Temperature Phase of Formamidinium Lead Iodide. *J. Phys. Chem. Lett.* **2015**, *6* (7), 1249–1253. https://doi.org/10.1021/acs.jpclett.5b00380.

(27) McMeekin, D. P.; Sadoughi, G.; Rehman, W.; Eperon, G. E.; Saliba, M.; Hörantner, M. T.; Haghighirad, A.; Sakai, N.; Korte, L.; Rech, B.; et al. A Mixed-Cation Lead Mixed-Halide Perovskite Absorber for Tandem Solar Cells. *Science (80-.).* **2016**, *351* (6269), 151–155. https://doi.org/10.1126/science.aad5845.

(28) Boyd, C. C.; Cheacharoen, R.; Leijtens, T.; McGehee, M. D. Understanding Degradation Mechanisms and Improving Stability of Perovskite Photovoltaics. *Chem. Rev.* **2019**, *119* (5), 3418–3451. https://doi.org/10.1021/acs.chemrev.8b00336.

(29) Habisreutinger, S. N.; Leijtens, T.; Eperon, G. E.; Stranks, S. D.; Nicholas, R. J.; Snaith, H. J. Carbon Nanotube/Polymer Composites as a Highly Stable Hole Collection Layer in Perovskite Solar Cells. *Nano Lett.* **2014**, *14* (10), 5561–5568.

https://doi.org/10.1021/nl501982b.

(30) Bryant, D.; Aristidou, N.; Pont, S.; Sanchez-Molina, I.; Chotchunangatchaval, T.; Wheeler, S.; Durrant, J. R.; Haque, S. A. Light and Oxygen Induced Degradation Limits the Operational Stability of Methylammonium Lead Triiodide Perovskite Solar Cells. *Energy Environ. Sci.* **2016**, *9* (5), 1655–1660. https://doi.org/10.1039/c6ee00409a.

(31) Pearson, A. J.; Eperon, G. E.; Hopkinson, P. E.; Habisreutinger, S. N.; Wang, J. T. W.; Snaith, H. J.; Greenham, N. C. Oxygen Degradation in Mesoporous Al2O3/CH3NH3PbI3-XClx Perovskite Solar Cells: Kinetics and Mechanisms. *Adv. Energy Mater.* **2016**, *6* (13), 1–10. https://doi.org/10.1002/aenm.201600014.

(32) Aristidou, N.; Eames, C.; Sanchez-Molina, I.; Bu, X.; Kosco, J.; Saiful Islam, M.; Haque, S. A. Fast Oxygen Diffusion and Iodide Defects Mediate Oxygen-Induced Degradation of Perovskite Solar Cells. *Nat. Commun.* **2017**, *8* (May), 1–10. https://doi.org/10.1038/ncomms15218.

(33) Kim, G. Y.; Senocrate, A.; Yang, T. Y.; Gregori, G.; Grätzel, M.; Maier, J. Large Tunable Photoeffect on Ion Conduction in Halide Perovskites and Implications for Photodecomposition. *Nat. Mater.* **2018**, *17* (5), 445–449. https://doi.org/10.1038/s41563-018-0038-0.

(34) Walsh, A.; Scanlon, D. O.; Chen, S.; Gong, X. G.; Wei, S. H. Self-Regulation Mechanism for Charged Point Defects in Hybrid Halide Perovskites. *Angew. Chemie - Int. Ed.* **2015**, *54* (6), 1791–1794. https://doi.org/10.1002/anie.201409740.

(35) Hoke, E. T.; Slotcavage, D. J.; Dohner, E. R.; Bowring, A. R.; Karunadasa, H. I.; McGehee, M. D. Reversible Photo-Induced Trap Formation in Mixed-Halide Hybrid Perovskites for Photovoltaics. *Chem. Sci.* **2015**, *6* (1), 613–617. https://doi.org/10.1039/c4sc03141e.

(36) Tsai, H.; Asadpour, R.; Blancon, J. C.; Stoumpos, C. C.; Durand, O.; Strzalka, J. W.; Chen, B.; Verduzco, R.; Ajayan, P. M.; Tretiak, S.; et al. Light-Induced Lattice Expansion Leads to High-Efficiency Perovskite Solar Cells. *Science (80-.).* **2018**, *360* (6384), 67–70. https://doi.org/10.1126/science.aap8671.

(37) DeQuilettes, D. W.; Zhang, W.; Burlakov, V. M.; Graham, D. J.; Leijtens, T.; Osherov, A.; Bulović, V.; Snaith, H. J.; Ginger, D. S.; Stranks, S. D. Photo-Induced Halide Redistribution in Organic-Inorganic Perovskite Films. *Nat. Commun.* **2016**, *7* (May). https://doi.org/10.1038/ncomms11683.

(38) Eperon, G. E.; Leijtens, T.; Bush, K. A.; Prasanna, R.; Green, T.; Wang, J. T. W.; McMeekin, D. P.; Volonakis, G.; Milot, R. L.; May, R.; et al. Perovskite-Perovskite Tandem Photovoltaics with Optimized Band Gaps. *Science (80-.).* **2016**, *354* (6314), 861–865. https://doi.org/10.1126/science.aaf9717.

(39) Hörantner, M. T.; Leijtens, T.; Ziffer, M. E.; Eperon, G. E.; Christoforo, M. G.; McGehee, M.

D.; Snaith, H. J. The Potential of Multijunction Perovskite Solar Cells. *ACS Energy Lett.* **2017**, *2* (10), 2506–2513. https://doi.org/10.1021/acsenergylett.7b00647.

(40) Bush, K. A.; Palmstrom, A. F.; Yu, Z. J.; Boccard, M.; Cheacharoen, R.; Mailoa, J. P.; McMeekin, D. P.; Hoye, R. L. Z.; Bailie, C. D.; Leijtens, T.; et al. 23.6%-Efficient Monolithic Perovskite/Silicon Tandem Solar Cells With Improved Stability. *Nat. Energy* **2017**, *2* (4), 1–7. https://doi.org/10.1038/nenergy.2017.9.

(41) Braly, I. L.; Hillhouse, H. W. Optoelectronic Quality and Stability of Hybrid Perovskites from MAPbI3 to MAPbI2Br Using Composition Spread Libraries. *J. Phys. Chem. C* **2016**, *120* (2), 893–902. https://doi.org/10.1021/acs.jpcc.5b10728.

(42) Hillhouse, H. W.; Beard, M. C. Solar Cells from Colloidal Nanocrystals: Fundamentals, Materials, Devices, and Economics. *Curr. Opin. Colloid Interface Sci.* **2009**, *14* (4), 245–259. https://doi.org/10.1016/j.cocis.2009.05.002.

(43) Stoddard, R. J.; Eickemeyer, F. T.; Katahara, J. K.; Hillhouse, H. W. Correlation between Photoluminescence and Carrier Transport and a Simple in Situ Passivation Method for High-Bandgap Hybrid Perovskites. *J. Phys. Chem. Lett.* **2017**, *8* (14), 3289–3298. https://doi.org/10.1021/acs.jpclett.7b01185.

(44) Chen, Q.; De Marco, N.; Yang, Y.; Song, T. Bin; Chen, C. C.; Zhao, H.; Hong, Z.; Zhou, H.; Yang, Y. Under the Spotlight: The Organic-Inorganic Hybrid Halide Perovskite for Optoelectronic Applications. *Nano Today* **2015**, *10* (3), 355–396. https://doi.org/10.1016/j.nantod.2015.04.009.

(45) Wang, Q.; Zheng, X.; Deng, Y.; Zhao, J.; Chen, Z.; Huang, J. Stabilizing the α-Phase of CsPbI3 Perovskite by Sulfobetaine Zwitterions in One-Step Spin-Coating Films. *Joule* **2017**, *1* (2), 371–382. https://doi.org/10.1016/j.joule.2017.07.017.

(46) Charles, F. F.; David, G. B. Control of Humidity in Small Controlled-environment Chambers using Glycerol-water Solution. HortTechnology horttech, 2(1), 52-54 https://doi.org/10.21273/horttech.2.1.52.

(47) Rajakumar, T. M.; Sanjeeviraja, C.; Chandramani, R. Spectro-Structural Characterization of Chalcogenide Films Containing Cd, Te and Se. *J. Miner. Mater. Charact. Eng.* **2011**, *10* (11), 1051–1060. https://doi.org/10.4236/jmmce.2011.1011080.

(48) Viezbicke, B. D.; Patel, S.; Davis, B. E.; Birnie, D. P. Evaluation of the Tauc Method for Optical Absorption Edge Determination: ZnO Thin Films as a Model System. *Phys. Status Solidi Basic Res.* **2015**, *252* (8), 1700–1710. https://doi.org/10.1002/pssb.201552007.

(49) Marronnier, A.; Roma, G.; Boyer-Richard, S.; Pedesseau, L.; Jancu, J. M.; Bonnassieux, Y.; Katan, C.; Stoumpos, C. C.; Kanatzidis, M. G.; Even, J. Anharmonicity and Disorder in the Black Phases of Cesium Lead Iodide Used for Stable Inorganic Perovskite Solar Cells. *ACS Nano* **2018**, *12* (4), 3477–3486. https://doi.org/10.1021/acsnano.8b00267.